

BROCK UNIVERSITY LIBRARY



3 9157 00931471 0







# Optical Properties of Organic Superconductor

$\kappa\text{-(BETS)}_2\text{FeBr}_4$

by

Nazanin Hossein khah

A THESIS SUBMITTED IN PARTIAL FULFILMENT OF  
THE REQUIREMENTS FOR THE DEGREE OF

MASTER OF SCIENCE

in

The Faculty of Mathematics and Sciences

Department of Physics



BROCK UNIVERSITY

December 21, 2006

2006 © Nazanin Hossein khah



In presenting this thesis in partial fulfilment of the requirements for an advanced degree at the Brock University, I agree that the Library shall make it freely available for reference and study. I further agree that permission for extensive copying of this thesis for scholarly purposes may be granted by the head of my department or by his or her representatives. It is understood that copying or publication of this thesis for financial gain shall not be allowed without my written permission.

(Signature) \_\_\_\_\_

Department of Physics

Brock University  
St.Catharines, Canada

Date \_\_\_\_\_





# Abstract

$\kappa$ -(BETS)<sub>2</sub>FeBr<sub>4</sub> is a quasi-2D charge transfer organic metal with interesting electronic and magnetic properties. It undergoes a transition to an antiferromagnetic (AF) state at ambient pressure at the Néel temperature ( $T_N$ ) = 2.5 K, as well as to a superconducting (SC) state at 1.1 K [1].

The temperature dependence of the electrical resistivity shows a small decrease at  $T_N$  indicating the resistivity drops as a result of the onset of the ordering of Fe<sup>3+</sup> spins. A sharp drop in the resistivity at 1.1 K is due to its superconducting transition. The temperature dependence of the susceptibility indicates an antiferromagnetic spin structure with the easy axis parallel to the  $a$ -axis. The specific heat at zero-field shows a large peak at about 2.4 K, which corresponds to the antiferromagnetic transition temperature ( $T_N$ ) and no anomaly is observed around the superconducting transition temperature (1.1 K) demonstrating that the magnetically ordered state is not destroyed by the appearance of another phase transition (the superconducting transition) in the  $\pi$ -electron layers [1], [2].

This work presents an investigation of how the low frequency electromagnetic response is affected by the antiferromagnetic and superconducting states, as well as the onset of strong correlation. The location of the easy axis of three samples was determined and polarized thermal reflectance measurements of these  $\kappa$ -(BETS)<sub>2</sub>FeBr<sub>4</sub> samples oriented with their vertical axis along the  $a$ - and  $c$  axes were then carried out using a <sup>3</sup>He refrigerator cryostat and a Martin-Puplett type polarizing interferometer at various temperatures ( $T$  = 0.5 K, 1.4 K, 1.9 K, 2.8 K) above and below the superconducting state and/or antiferromagnetic state.

Comparison of the SC state to the normal state along the  $a$ - and  $c$ -axes indicates a rising thermal reflectance at low frequencies (below 10 cm<sup>-1</sup>) which may be a manifestation of the superconducting energy gap. A dip-like feature is detected at low frequencies (below 15 cm<sup>-1</sup>) in the thermal reflectance plots which probe the antiferromagnetic state along the two axes, and may be due to



the opening of a gap in the excitation spectrum as a result of the antiferromagnetism.

In another set of experiments, thermal reflectance measurements carried out along the  $a$ - and  $c$ -axes at higher temperatures (10 K-80 K) show that the reflectivity decreases with increasing temperature to 60 K (the coherence temperature) above which it increases again. Comparison of the thermal reflectance plots along the  $a$ - and  $c$ -axes at higher temperatures reveals an anisotropy between these two axes.

The Hagen-Rubens thermal reflectance plots corresponding to an average over the  $ac$ -plane were calculated using experimental literature resistivity values. Comparison of the Hagen-Rubens plots with the experimental thermal reflectance along the  $a$ - and  $c$ -axes indicates that both exhibit the general trend of a decrease in thermal reflectance with increasing frequency, however the calculated Hagen-Rubens thermal reflectance at different temperatures is much lower than the experimental curves.



# Contents

|  |           |
|--|-----------|
| Abstract . . . . .   | ii        |
| Contents . . . . .   | iv        |
| List of Tables . . . . .   | vi        |
| List of Figures . . . . .  | vii       |
| Acknowledgements . . . . .   | ix        |
| <b>1 Introduction to Organic Superconductors . . . . .</b>   | <b>1</b>  |
| 1.1 $\kappa$ -(BETS) <sub>2</sub> FeBr <sub>4</sub> . . . . .  | 2         |
| 1.1.1 Crystal Structure . . . . .  | 3         |
| 1.1.2 Electronic Structure . . . . .   | 5         |
| 1.1.3 Magnetic Properties . . . . .  | 8         |
| 1.1.4 Temperature Dependence of the Specific Heat of $\kappa$ -(BETS) <sub>2</sub> FeBr <sub>4</sub> . . . . . | 8         |
| <b>2 Electronic Band Structure and Superconductivity . . . . .</b>   | <b>13</b> |
| 2.1 Band Structure . . . . .   | 13        |
| 2.2 Conventional Superconductivity . . . . .   | 16        |
| 2.3 Unconventional superconductors . . . . .   | 18        |
| 2.3.1 Electronic Structure and Optical Properties of Unconventional Superconductors                            | 18        |
| 2.3.2 Electron-phonon coupling . . . . .   | 21        |
| <b>3 Experimental setup . . . . .</b>  | <b>24</b> |
| 3.1 Martin-Puplett Interferometer: . . . . .   | 24        |



---

|          |   |           |
|----------|---|-----------|
| 3.2      | The Helium-3 Cryostat: . . . . .  | 25        |
| 3.3      | Sample preparation: . . . . .   | 29        |
| 3.4      | Thermal Reflectance . . . . .   | 31        |
| <b>4</b> | <b>Results . . . . .</b>  | <b>32</b> |
| 4.1      | Optical results for the $\kappa$ -(BETS) <sub>2</sub> FeBr <sub>4</sub> samples . . . . . | 32        |
| 4.2      | Hagen-Rubens Calculation . . . . .  | 41        |
| <b>5</b> | <b>Conclusions . . . . .</b>  | <b>45</b> |
|          | <b>Bibliography . . . . .</b>   | <b>47</b> |





---

# List of Tables

|     |  |   |
|-----|--|---|
| 1.1 | Overlap integrals, mid gaps energies, and bandwidths of the upper band for $\kappa$ -<br>(BETS) <sub>2</sub> FeBr <sub>4</sub> . . . . . | 6 |
|-----|--|---|



# List of Figures

|     |  |    |
|-----|--|----|
| 1.1 | Structure of BETS molecules. . . . .   | 3  |
| 1.2 | Crystal Structure of $\kappa$ -(BETS) <sub>2</sub> FeBr <sub>4</sub> . . . . .   | 4  |
| 1.3 | Molecular Structure of BETS radical cation and the $FeBr_4^-$ anion. . . . .   | 5  |
| 1.4 | Band structure and fermi surface of $\kappa$ -(BETS) <sub>2</sub> FeBr <sub>4</sub> . . . . .                                  | 6  |
| 1.5 | Electrical Resistivity. . . . .  | 7  |
| 1.6 | Temperature dependence of the magnetic susceptibility in paramagnets, ferromagnets<br>and antiferromagnets. . . . .            | 9  |
| 1.7 | Magnetic susceptibility of $\kappa$ -(BETS) <sub>2</sub> FeBr <sub>4</sub> at 500 Oe. . . . .                                  | 10 |
| 1.8 | Specific Heat. . . . .   | 11 |
| 2.1 | The distinction between insulators, semiconductors and metals. . . . .   | 14 |
| 2.2 | Electronic Band structure. . . . .   | 15 |
| 2.3 | Reflectance and Thermal reflectance of BCS superconductors. . . . .  | 17 |
| 2.4 | Reflectance and conductivity spectra for $\beta$ -(ET) <sub>2</sub> I <sub>3</sub> . . . . .                                   | 20 |
| 3.1 | Martin-Puplett Interferometer. . . . .   | 25 |
| 3.2 | The Helium-3 Cryostat (Top View). . . . .  | 26 |
| 3.3 | The Helium-3 Cryostat (Side View). . . . .   | 27 |
| 3.4 | $\kappa$ -(BETS) <sub>2</sub> FeBr <sub>4</sub> sample pieces. . . . .   | 29 |
| 3.5 | Reflectance versus Frequency for different orientations. . . . .   | 30 |
| 4.1 | Plots of intensity versus angle to find the easy axis. . . . .   | 33 |
| 4.2 | $\kappa$ -(BETS) <sub>2</sub> FeBr <sub>4</sub> samples on the copper block. . . . .   | 34 |
| 4.3 | Thermal reflectance of $\kappa$ -(BETS) <sub>2</sub> FeBr <sub>4</sub> samples versus wave number along the $a$ -axis. . . . . | 36 |



---

|     |  |    |
|-----|--|----|
| 4.4 | Thermal reflectance of $\kappa$ -(BETS) <sub>2</sub> FeBr <sub>4</sub> samples versus wave number along the $c$ -axis. | 38 |
| 4.5 | The thermal reflectance at different temperatures along the $a$ -axis. . . . .   | 39 |
| 4.6 | The thermal reflectance at different temperatures along the $c$ -axis. . . . .   | 40 |
| 4.7 | Comparison of the thermal reflectance curves along the $a$ - and $c$ -axes at a specific temperature. . . . .          | 42 |
| 4.8 | Hagen-Rubens thermal reflectance calculation at different temperatures. . . . .  | 44 |



# Acknowledgements

With gratitude, I wish to express my sincere thanks to my supervisor Dr. Maureen Reedyk for her support, guidance and patience. Her helpful advice through the steps of the experiments and data analysis is truly appreciated.

Special thanks to G. V. Sudhakar Rao for his great help, comments and support during the long hours of experiment.

I would like to thank my committee members, Dr. David Crandles and Dr. Kirill Samokhin and also thanks to all faculty members in the department.

Thanks to my persian friends and laboratory group fellows for making the school a peaceful and friendly place.

I am thankful to Sheila and her family for their continuous support and kindness.

I wish to express my warm and sincere thanks to my parents and my sister, who I have missed a lot. They have always been there for me and rendered me enormous support.

I feel a deep sense of gratitude for my aunt who has been very supportive, and helpful in every aspect which made my life easier.

Lastly, my very special thanks to my fiance, Omid who I have missed a lot, for his love, support, and useful advice.

Finally, I would like to thank all whose direct and indirect support helped me completing my thesis in time.





# Chapter 1

## Introduction to Organic Superconductors

Organic materials such as organic polymers, are generally regarded as good insulators. More recent developments in material science and technology, however, have brought about the discovery of organic conductors such as organic metals and even superconductors. The properties of materials such as ordinary metals and superconductors have generally been well described by the theories of solid state physics.

For organic materials the molecular properties specify the electronic properties in the solid state [3]. Organic conductors consist of open-shell molecular units which are the result of partial oxidation and reduction of donor and acceptor molecules in the crystal-growth process. It is the unpaired electron residing in the  $\pi$ -molecular orbital ( $\pi$ -hole) of the donor unit which is responsible for the electronic properties of these charge-transfer organic materials. Due to a  $\pi$ -orbital overlap between adjacent molecules, the  $\pi$ -holes can delocalize throughout the crystal giving rise to metallic conductivity.

The unique chemistry of carbon, which, on the one hand, provides a rich basis of potential organic donor molecules, and the manifold possibilities of combining them with charge-compensating acceptor units, on the other, have enabled the synthesis of an enormous number of conducting organic charge-transfer salts. The geometry of the building blocks (bricks) and the way they are packed together in the crystal determine the effective dimensionality of the electronic structure of the compound. The planar shape of the TMTSF (tetramethyltetraselenafulvalene) molecule - a derivative of the prototype TTF (tetrathiafulvalene) - permits an infinite stacking of these units in the crystal structure. As a consequence, a significant intermolecular overlap of the  $\pi$ -orbitals occurs only along the stacking axis giving rise to a *quasi one-dimensional* conduction band. In contrast, packing of the larger BEDT-TTF (bisethylenedithio-tetrathiafulvalene) molecules (commonly abbreviated as ET) often results in a *quasi two-dimensional* electronic structure [4].



From structural aspects, the rather loose intra-stack coupling of the  $(\text{BEDT-TTF})_2X$  salts gives rise to a variety of polymorphic phases (packing motifs) which are distinguished by Greek characters: the most important among them are the  $\alpha$ -,  $\beta$ - and  $\kappa$ -phases.

The  $\kappa$ -phase is unique in that it does not consist of interacting stacks but rather of interacting dimers formed by two face-to-face aligned ET molecules. Adjacent dimers are arranged almost orthogonal to each other so that the *intra*- and *inter*-dimer interactions are of the same size. This results in a quasi-2D electronic structure with a small in-plane anisotropy. The  $\kappa$ -type compounds with polymer-like anions are of particular interest with respect to their superconducting properties as they exhibit the highest transition temperatures [5].

## 1.1 $\kappa$ -(BETS) $_2\text{FeBr}_4$

The designability of organic systems has encouraged many chemists to produce completely new types of conducting systems. In contrast to the complicated molecular and crystal structures of organic conductors, their electronic structures are surprisingly simple. Investigations of Shubnikov-de Haas and de Haas-van Alphen oscillations (refers to the oscillatory behavior of the magnetoresistance of a metal as a function of magnetic field) have elucidated their simple Fermi surfaces<sup>1</sup>. Among the TTF derivatives synthesized so far, bis(ethylenedithio)-TTF (BEDT-TTF) has played the most important role in the development of organic conductors and has yielded many organic superconductors such as the  $\kappa$ -type BEDT-TTF superconductors, where transverse intermolecular S-S networks play an essential role in forming a two-dimensional Fermi surface (Fig. 1.1).

$\kappa$ -(BETS) $_2\text{FeBr}_4$  salt [where BETS = bis(ethylenedithio)-tetraselenafulvalene] is the first anti-ferromagnetic organic metal at ambient pressure ( $T_N = 2.5$  K). A small resistivity drop has been observed by Fujiwara *et al.* at  $T_N$  which clearly shows the existence of the interaction between  $\pi$

---

<sup>1</sup>The Shubnikov-de Haas (SdH) effect is a magnetotransport phenomena that occurs in metals in an intense magnetic field and its effect is similar to the de Haas-van Alphen effect in that the signature of the effect is a periodic waveform when plotted as a function of inverse magnetic field ( $1/H$ ). The "frequency" of the magnetoresistance (which is the property of some materials to change the value of their electrical resistance when an external magnetic field is applied to them) oscillations (in inverse field space) indicates the area of the extremal Fermi surface. The area of the Fermi surface is expressed in tesla [6], [?].



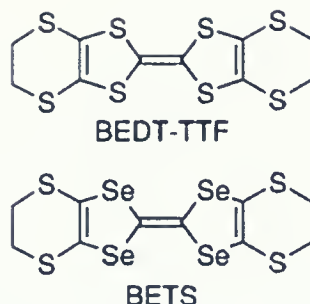


Figure 1.1: Structure of BETS molecules [1].

metal electrons and localized magnetic moments of  $\text{Fe}^{3+}$  ions. In addition, this system undergoes a superconducting transition at 1.1 K. Thus,  $\kappa\text{-(BETS)}_2\text{FeBr}_4$  is the first antiferromagnetic organic metal exhibiting a superconducting transition below the Néel temperature [1].

### 1.1.1 Crystal Structure

$\kappa\text{-(BETS)}_2\text{FeBr}_4$  forms in rhombus shaped samples. The  $ac$ -plane is the two dimensional conduction plane with the  $a$ -axis as its *easy axis* - which refers to the energetically favorable direction of the spontaneous magnetization in a ferromagnetic material. For these samples, the  $a$ -axis is oriented along the long diagonal of the rhombus and the  $c$ -axis is aligned perpendicular to it.

Fujiwara *et al.* made plate-shaped crystals electrochemically from a 10% ethanol-chlorobenzene solution containing BETS and tetraethylammonium iron(III) tetrabromide with a constant current of  $0.7\ \mu\text{A}$  applied for 2-4 weeks at room temperature or  $40\ ^\circ\text{C}$ . Figure 1.2 shows the crystal structure of this salt determined at room temperature.

One BETS molecule and one-half of the  $\text{FeBr}_4^-$  anion are crystallographically independent, and the  $\text{FeBr}_4^-$  anion is on a mirror plane. The molecular structures of the BETS radical cation and  $\text{FeBr}_4^-$  anion at room temperature are shown in Fig. 1.3. The BETS molecule has a slightly non-planar molecular structure. As shown in Fig. 1.2, the BETS molecules form dimers and adjacent BETS dimers are arranged in a roughly orthogonal manner characteristic of the  $\kappa$ -type packing motif.

The analyses of the BETS intermolecular distances show that there is only one Se-Se type short contact ( $<3.80\ \text{\AA}$ ),  $3.796\ \text{\AA}$  [c1: Se(1)-Se(2)], and the shortest Se-S and S-S distances are  $3.593\ \text{\AA}$  [c2:



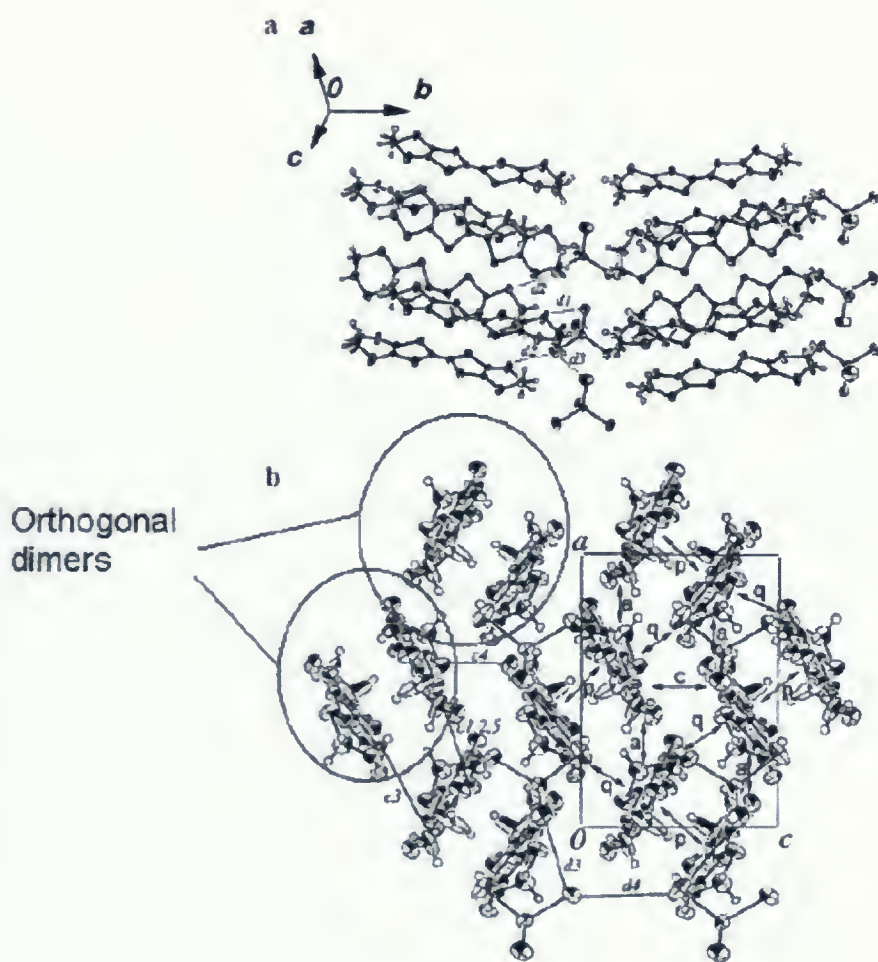


Figure 1.2: Crystal Structure of  $\kappa$ -(BETS)<sub>2</sub>FeBr<sub>4</sub>, (a) Crystal structure of  $\kappa$ -(BETS)<sub>2</sub>FeBr<sub>4</sub>.

(b) Projection along the *b*-axis. The short chalcogen-chalcogen contacts: *c1* [Se(1)-Se(2)] = 3.796, *c2* [Se(3)-S(4)] = 3.593, *c3* [Se(1)-S(4)] = 3.656, *c4* [S(1)-S(3)] = 3.362, and *c5* [S(1)-S(2)] = 3.369 Å. The short distances: *d1* [Br(3)-S(2)] = 3.693, *d2* [Br(1)-S(3)] = 3.708, *d3* [Br(1)-Br(3)] = 4.137, and *d4* [Br(2)-Br(3)] = 4.637 Å. The overlap integrals: *p* 77.33, *a* -22.41, *c* 35.14, and *q*  $8.11 \times 10^{-3}$ . From Fujiwara *et al.* [1]





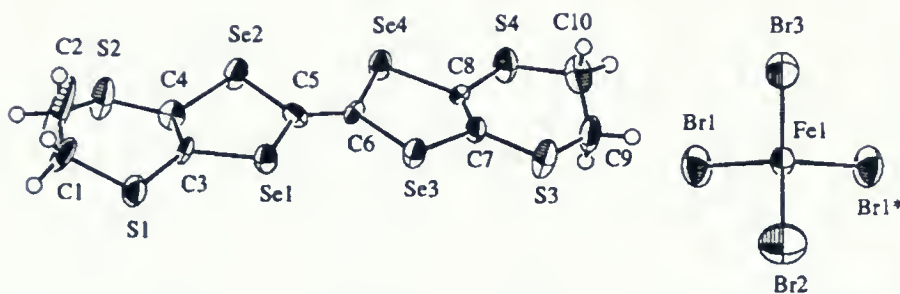


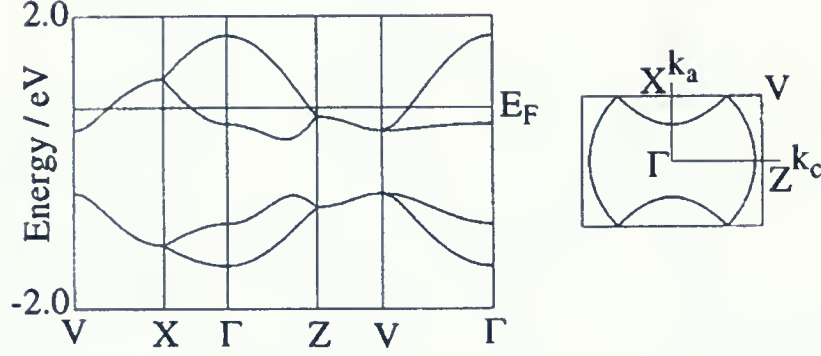
Figure 1.3: Molecular Structure of BETS radical cation and the  $\text{FeBr}_4^-$  anion with the labeling of the atoms at room temperature [1].

$\text{Se}(3)\text{-S}(4)]$  and  $3.362 \text{ \AA}$  [ $c4: \text{S}(1)\text{-S}(3)$ ], respectively [1]. Two-dimensional conduction layers (the *ac*-plane) composed of the BETS dimers and insulating layers of tetrahedral anions with localized magnetic  $\text{Fe}^{3+}$  moments are arranged alternately along the *b* direction (Figures 1.2 and 1.3). In the anion layer, the shortest Fe-Fe distance is  $5.921 \text{ \AA}$  along the *a*-axis and  $8.504 \text{ \AA}$  along the *c*-axis. Between the  $\text{FeBr}_4^-$  anion molecules, the shortest Br-Br distance along the *a*-axis is  $4.137 \text{ \AA}$  [ $d3: \text{Br}(1)\text{-Br}(3)$ ], which is much shorter than that along the *c*-axis,  $4.637 \text{ \AA}$  [ $d4: \text{Br}(2)\text{-Br}(3)$ ]; however, these distances are still longer than the sum of the van der Waals radii of bromines ( $3.7 \text{ \AA}$ ). From these results the direct intermolecular interaction between the  $\text{FeBr}_4^-$  anion molecules is considered to be weak but relatively stronger along the *a*-axis than along the *c*-axis. There are several short Br-S contacts almost equal to the sum of the van der Waals radii of bromine and sulfur atoms ( $3.7 \text{ \AA}$ ) between BETS and the anion molecules as indicated in Fig. 1.2. The shortest Br-S distance is  $3.693 \text{ \AA}$  [ $d1: \text{Br}(3)\text{-S}(2)$ ] [?].

### 1.1.2 Electronic Structure

Figure 1.4 shows the band dispersion and Fermi surface calculated according to the crystal structure at room temperature by Fujiwara *et al* (See section 2.2.1 for a summary of the procedure).



Figure 1.4: Band structure and fermi surface of  $\kappa$ -(BETS) $_2$ FeBr $_4$  [1].

|                                 | a                       | p                      | q                     | c                      | E mid-gap | bandwidth |
|---------------------------------|-------------------------|------------------------|-----------------------|------------------------|-----------|-----------|
| $\kappa$ -(BETS) $_2$ FeBr $_4$ | $-22.41 \times 10^{-3}$ | $77.33 \times 10^{-3}$ | $8.11 \times 10^{-3}$ | $35.14 \times 10^{-3}$ | 0.68      | 1.44      |

Table 1.1: Overlap integrals, mid gaps energies, and bandwidths of the upper band [7].

Table 1.1 shows the calculated [7] overlap integrals (The integral defining the summation over the space of the overlap of the electron density of two orbitals), mid-gap energies, and the bandwidth of the upper band of  $\kappa$ -(BETS) $_2$ FeBr $_4$ . The intradimer overlap integral ( $p = 77.33 \times 10^{-3}$ ) of the  $\kappa$ -(BETS) $_2$ FeBr $_4$  salt is much larger than the other overlaps ( $a = -22.41 \times 10^{-3}$ ;  $q = 8.11 \times 10^{-3}$ ; and  $c = 35.14 \times 10^{-3}$ ) reflecting the dimer structure of the  $\kappa$ -type salts. The band dispersion of  $\kappa$ -(BETS) $_2$ FeBr $_4$  has four energy branches corresponding to the existence of four donor molecules in one unit of the donor sheet. There is a mid-gap between the upper two branches and the lower two branches due to the strong dimerization of the donor molecules as is often observed in  $\kappa$ -type BEDT-TTF salts and the upper band is effectively half-filled consequently. The energy of the mid-gap of the  $\kappa$ -(BETS) $_2$ FeBr $_4$  salt is 0.68 eV, which is much larger than that of the  $\kappa$ -(BETS) $_2$ FeCl $_4$  salt (0.48 eV) corresponding to the comparatively larger strength of the intradimer interaction ( $p$ ), and suggesting stronger electron correlation in the  $\kappa$ -(BETS) $_2$ FeBr $_4$  salt. The Fermi surface of this salt is a two-dimensional circle closed at the XV boundary as a result of space group symmetry,



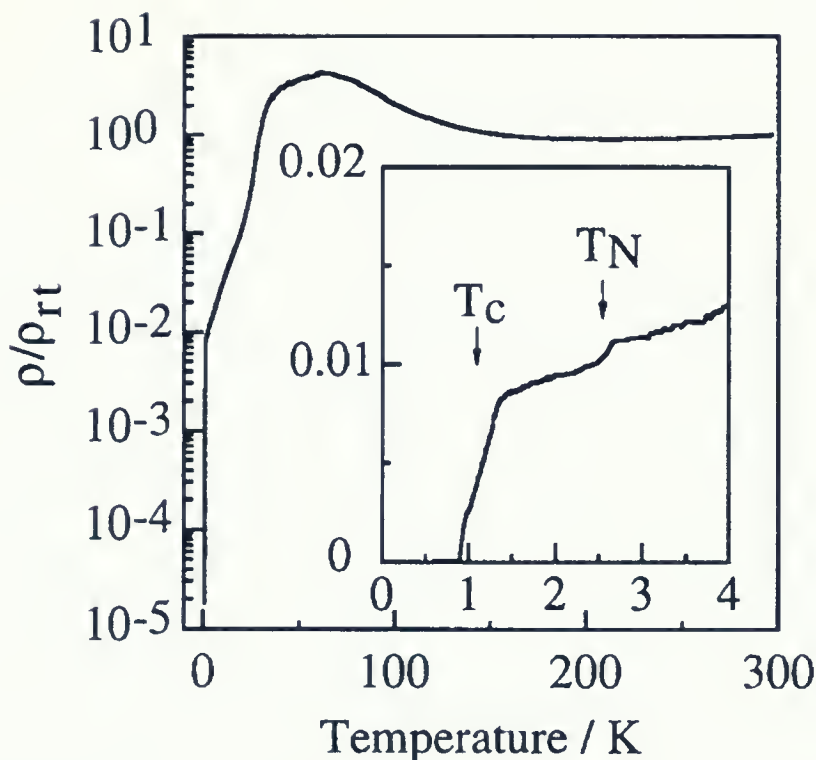


Figure 1.5: The temperature dependence of the electrical resistivity of  $\kappa$ -(BETS)<sub>2</sub>FeBr<sub>4</sub> at 0.6-300 K along the *ac*-plane in zero field. (Inset: Temperature range between 0.6 and 4 K [1].)

similar to those of the isostructural  $\kappa$ -(BETS)<sub>2</sub>FeCl<sub>4</sub> and  $\kappa$ -(BETS)<sub>2</sub>GaCl<sub>4</sub> salts which have been confirmed by Shubnikov-de Haas and de Haas-van Alphen oscillations (The quantum oscillations of conductivity).

The temperature dependence of the electrical resistivity of  $\kappa$ -(BETS)<sub>2</sub>FeBr<sub>4</sub> is shown in Fig. 1.5 which plots the electrical resistivity down to 0.6 K. The resistivity decreases very slowly down to about 200 K, then increases fairly sharply exhibiting a peak around 60 K (coherence temperature), below which is referred to as the "coherent regime" where the resistivity decreases very rapidly with decreasing temperature. Such a resistivity peak often has been observed in the  $\kappa$ -type BEDT-TTF superconducting salts and is considered to be a characteristic behavior for a strong electron correlation system having a strong intradimer interaction. Additionally, this resistivity peak may be associated with some structural transformations.

As seen from the inset of Figure 1.5, the resistivity shows a small drop at around 2.5 K where



the antiferromagnetic transition of the  $\text{Fe}^{3+}$  spins takes place. This clearly shows that the resistivity is depressed by the onset of the ordering of  $\text{Fe}^{3+}$  spins and can be regarded as direct evidence for the important role of the interaction between  $\pi$  metal electrons and localized magnetic moments [8]. The sharp drop in the resistivity at 1.1 K is attributed to its superconducting transition.

### 1.1.3 Magnetic Properties

In an antiferromagnet the spins are ordered in an antiparallel arrangement with zero net moment at temperatures below the ordering or Néel temperature. The susceptibility of an antiferromagnet is not infinite at  $T = T_N$ , but has a weak cusp as shown in Fig. 1.6 [9].

The magnetic susceptibility of  $\kappa\text{-(BETS)}_2\text{FeBr}_4$  was measured (by Fujiwara *et al.* [1]) by applying a magnetic field (500 Oe) along the three crystallographic axes of the single crystal (the a, b, and c-axes). The magnetic susceptibilities obtained for 100-300 K (Fig. 1.7) can be well fitted by a Curie-Weiss plot, where  $\chi T$  is almost constant:  $\chi = C/(T-\theta)$ , where  $C = 4.70 \text{ K emu mol}^{-1}$  and  $\theta = -5.5 \text{ K}$ . This negative Weiss temperature  $\theta = -5.5 \text{ K}$  suggests the dominant magnetic interaction to be antiferromagnetic [10]. As shown by comparison with Fig. 1.6, the temperature dependence of the susceptibility of an antiferromagnetic material is consistent with the susceptibility obtained in Fig. 1.7 with a peak at  $T_N = 2.5 \text{ K}$  [3].

### 1.1.4 Temperature Dependence of the Specific Heat of

#### $\kappa\text{-(BETS)}_2\text{FeBr}_4$

$\kappa\text{-(BETS)}_2\text{FeBr}_4$  salt shows a transition from an antiferromagnetic metal phase to a superconducting state. It is of considerable interest to study whether the antiferromagnetic spin ordering and superconductivity coexist below the Néel temperature. To confirm the bulk nature of the phase transitions and to investigate the possibility of the coexistence of spin ordering and superconductivity at low temperatures, specific heat measurements were performed (Fig. 1.8) by the thermal relaxation method using a Helium-3 cryostat down to about 0.9 K by Fujiwara *et al.* [1], [11].

From Figure 1.8, it is clear that the specific heat,  $C_p$ , at zero-field shows a large anomaly characterized by a sharp  $\lambda$ -type peak at about 2.4 K, which corresponds to the antiferromagnetic





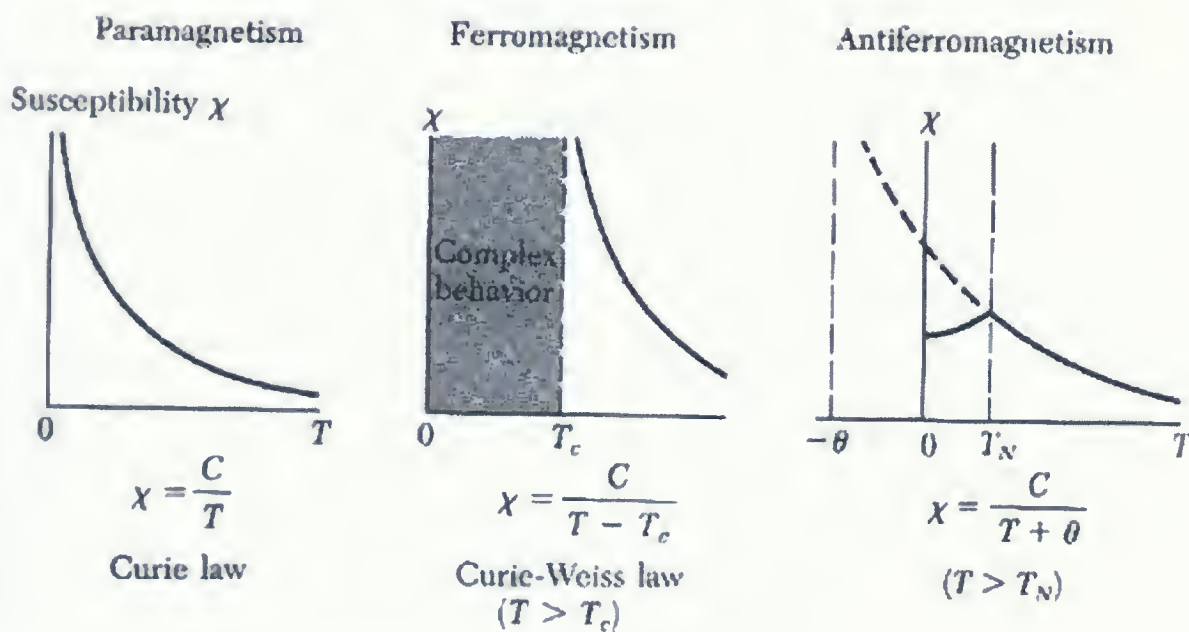


Figure 1.6: Temperature dependence of the magnetic susceptibility in paramagnets, ferromagnets and antiferromagnets [3]. Below the Néel temperature of an antiferromagnet the spins have antiparallel orientations; the susceptibility attains its maximum value at  $T_N$  where there is a well-defined kink in the curve of  $\chi$  versus  $T$ . The transition is also marked by a peak in the heat capacity.



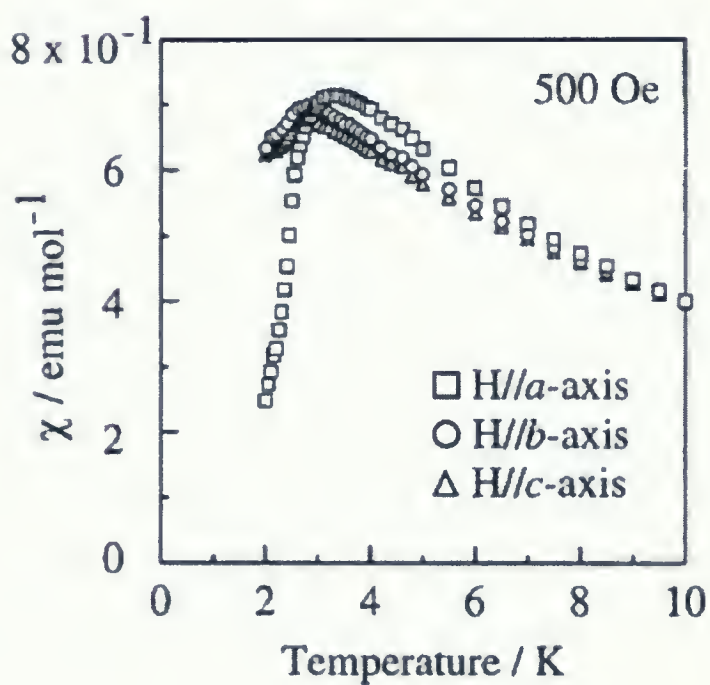


Figure 1.7: Magnetic susceptibility of  $\kappa$ -(BETS) $_2$ FeBr $_4$  at 500 Oe [1].  $\chi//a$  (open squares),  $\chi//b$  (open circles), and  $\chi//c$  (open triangles) represent the magnetic susceptibilities for the fields applied parallel to the crystallographic  $a$ -,  $b$ -, and  $c$ -axes, respectively.



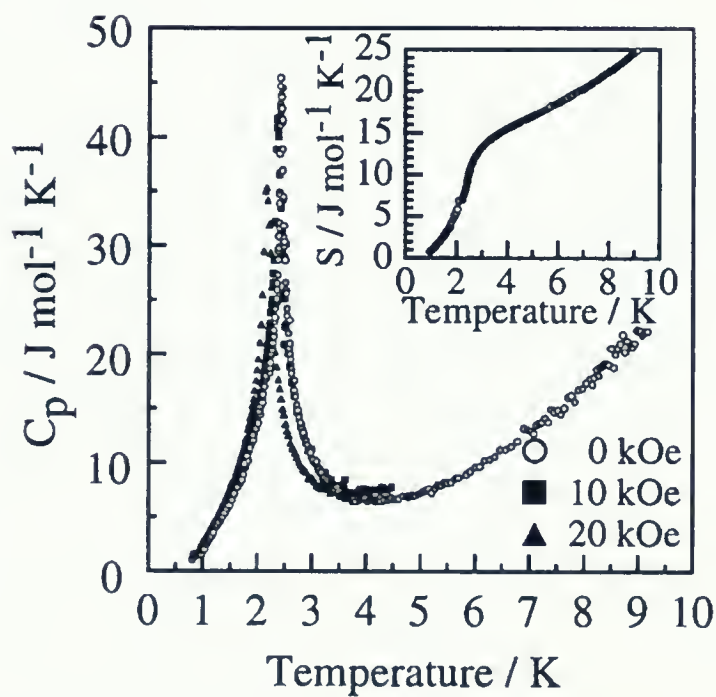


Figure 1.8: The temperature dependence of the zero-field specific heat of  $\kappa$ -(BETS) $_2$ FeBr $_4$  at 0.9-9 K. (Inset: The temperature dependence of the entropy distribution around the peak [1].)



transition temperature detected by the magnetic susceptibility and resistivity measurements. The integration of the  $C_p/T$  vs  $T$  curve with respect to temperature gives information on the entropy  $[S(T)]$  distribution around the peak, which is shown in the inset of Figure 1.8.

The magnetic results imply that the magnetic order is antiferromagnetic and that the spin state is the  $S = 5/2$  high-spin state of trivalent iron ions ( $\text{Fe}^{3+}$ ). In addition to this, no anomaly around the superconducting transition temperature (1.1 K) was detected, which demonstrates that the magnetically ordered state is not destroyed by the appearance of another phase transition, namely the superconducting transition in the  $\pi$ -electron layers. Therefore, it is possible to assert that the magnetic order and the superconductivity coexist at low temperatures below  $T_c = 1.1$  K. This is the first organic salt in which the long-range magnetic ordering of the magnetic anions mediated by  $\pi$ -donor molecules and the superconductivity based on the  $\pi$ -electrons in the donor layers coexist in the hybrid structure composed of the antiferromagnetic insulator and superconductor layers [12].

The goal of the work presented in this thesis is to investigate how the low frequency electromagnetic response is affected by the antiferromagnetic and superconducting states, as well as the onset of strong correlation. (This is discussed further in chapter 4).





## Chapter 2

# Electronic Band Structure and Superconductivity

### 2.1 Band Structure

The electronic band structure of a solid describes ranges of energy that an electron is forbidden or allowed to have. The band structure determines a material's electronic properties, optical properties, and a variety of other properties.

Every solid material has its own characteristic electronic band structure. According to this structure, the electrical behavior of solids can be explained. The wide range of electrical characteristics observed in various materials is due to variation in band structure. Depending on the energy difference between the conduction and valence band for instance the width of the forbidden energy band, solids are classified into the following categories (Figure 2.1):

**Insulators:** The valence electrons are tightly bound with the nucleus and free electrons are totally absent in an insulator. Very high energy is needed to separate them from the nucleus. Insulators have completely filled valence bands and conduction bands that are completely empty as shown in Figure 2.2. The energy gap is very large (up to 15 eV). Examples of insulators include mica, diamond and quartz.

**Semiconductors:** In semiconductors, an electron is loosely bound to the nucleus, hence less energy is needed to separate it from the nucleus. The difference between semiconductors and insulators is only that the forbidden band gap between the valence band and the conduction band is larger in an insulator, so that fewer electrons are found in the conduction band and the electrical conductivity is less. Also, the semiconductor only behaves as a metal at high temperature when carriers can be thermally excited to the conduction band. Therefore in semiconductors, a smaller amount of energy



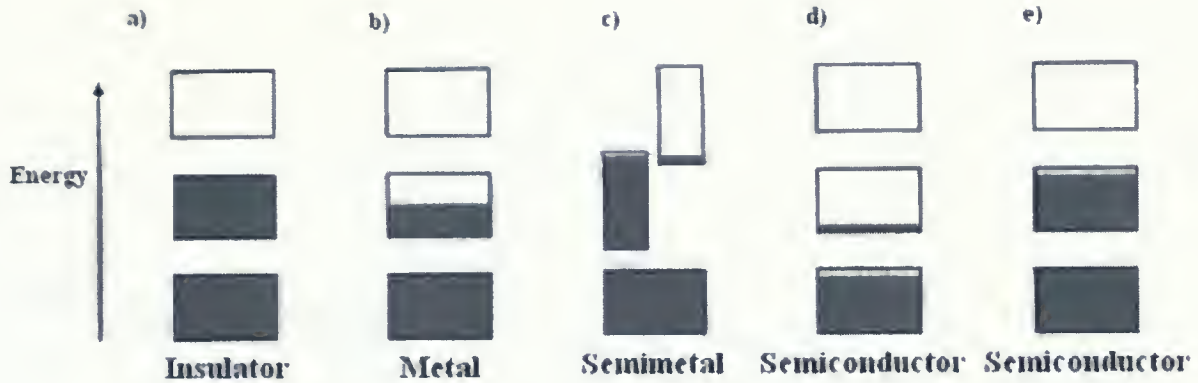


Figure 2.1: The distinction between insulators, semiconductors and metals. (a) insulator (wide band gap, filled valence band, empty conduction band). (b) metal (narrow band gap, filled valence band, partially filled conduction band). (c) semimetal (small overlap in the energy of the conduction band and valence bands i.e. Sn or graphite). (d) semiconductor (narrow band gap, slightly filled valence band). (e) semiconductor (narrow band gap, slightly empty conduction band).

is required to push the electrons from the valence band to the conduction band, thus making the semiconductor behave like a metal.

**Metals:** Metals have free or conduction electrons at room temperature. These electrons are free to move and hence take part in conduction. In conductors, the conduction bands are partially filled (Figure 2.2) or the valence band overlaps the conduction band and there is no energy band gap. Thus a large number of electrons are available. Free electrons contribute to the flow of current; holes are not created in the valence band.

Calculating band structures is an important topic in theoretical solid state physics. There are many models that are used to explain band structure (i.e. Nearly-free electron model, Kronig-Penney model and tight binding model). Each model describes some types of solids very well and others poorly. The nearly-free electron model works well for metals.

The optical conductivity of metals obeys the Drude model and decreases with increasing the frequency. Also the expected behavior of temperature dependence of dc conductivity ( $\sigma_{dc}$ ) is that the dc conductivity decreases as the temperature increases, since at low temperatures electrons are



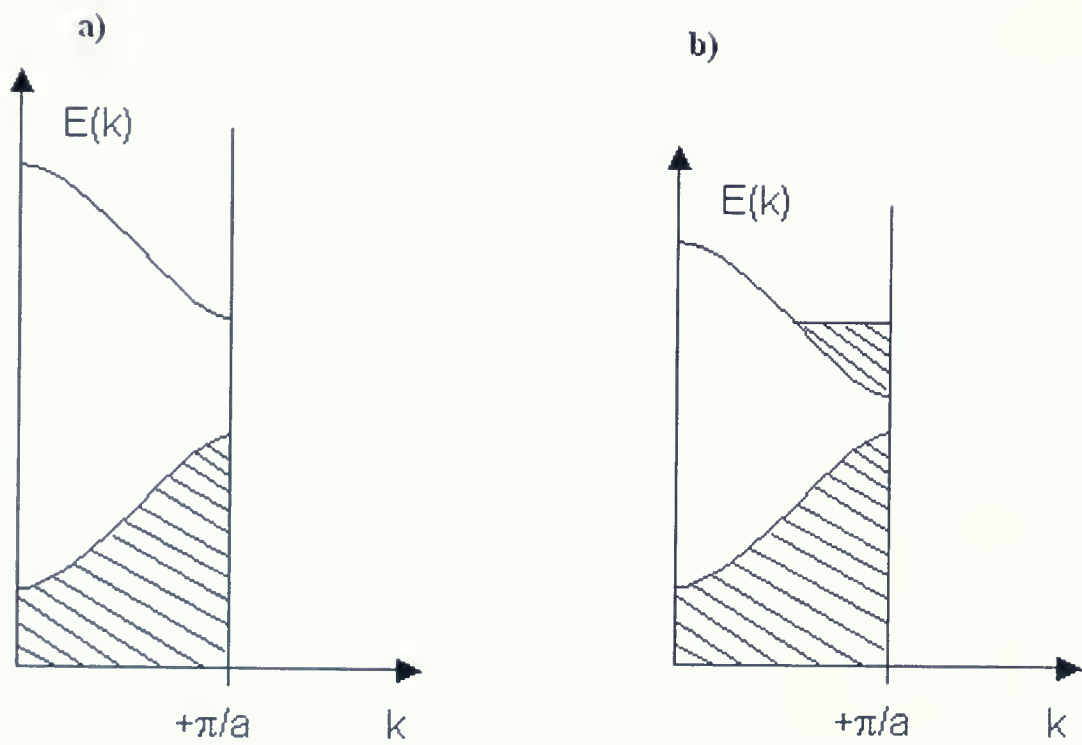


Figure 2.2: Band structure (a) insulator with completely filled valence bands and completely empty conduction bands, (b) metal with partially filled conduction bands.



able to move more freely with fewer interactions.

## 2.2 Conventional Superconductivity

Superconductivity is a phenomenon occurring in certain materials at extremely low temperatures, characterized by zero electrical resistance. The second defining property of a superconductor is that once the transition from the normal state to the superconducting state occurs, external magnetic fields cannot penetrate it (Meissner effect). In addition to repelling magnetic fields, enhanced thermal conductivity, higher optical reflectivity and reduced surface friction are also properties of superconductors.

The Meissner effect is the effect by which a weak magnetic field decays rapidly to zero in the interior of a superconductor. The distance to which weak magnetic field penetrates into a superconductor is known as the London penetration depth. It is found that the magnetic field is zero inside the material in the superconducting state regardless of what it was before the material became superconducting. As noted above the Meissner effect is one of the defining features of superconductivity, and its discovery established that the onset of superconductivity is a phase transition [13], [5].

In a superconductor below its transition temperature  $T_c$ , there is no resistance because the scattering mechanisms are unable to prevent the motion of the current carriers. The current is carried in all known classes of superconductors by pairs of electrons known as Cooper pairs. The mechanism by which two negatively charged electrons are bound together is well understood in conventional superconductors such as aluminium in terms of the mathematically complex BCS (Bardeen Cooper Schrieffer) theory [14].

The essential point is that below  $T_c$  the binding energy of a pair of electrons causes the opening of a gap in the energy spectrum at  $E_F$  (the Fermi energy - the highest occupied level in a solid), separating the pair states from the "normal" single electron states. The size of a Cooper pair is given by the coherence length which in conventional superconductors is typically 1000 Å [13]. The space occupied by one pair contains many other pairs, and there is thus a complex interdependence of the occupancy of the pair states. There is then insufficient thermal energy to scatter the pairs.





## BCS Superconductor

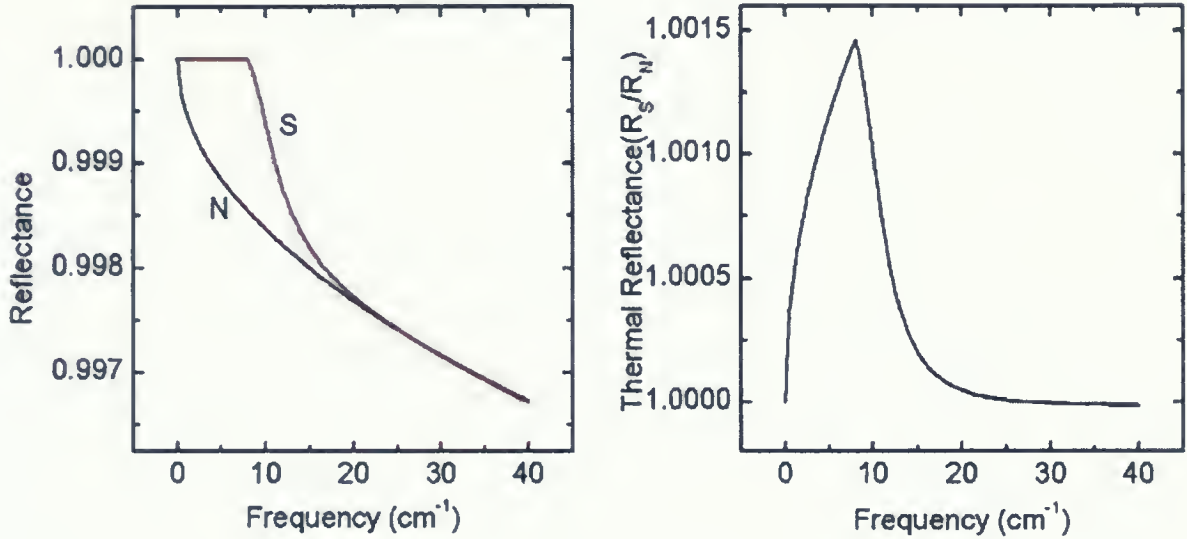


Figure 2.3: Reflectance and Thermal reflectance of BCS superconductors with an energy gap,  $2\Delta$  of width  $3.52 k_B T_c$ , and a dc-conductivity ( $\rho_{dc} = 2$  micro.ohm.cm) and a superconducting transition temperature ( $T_c = 1.6$  K) as parameters.

as reversing the direction of travel of one electron in the pair requires the destruction of the pair and many other pairs due to the nature of the many-electron BCS wavefunction. The pairs thus carry current without being impeded.

For the BCS superconductors, the optical functions, reflectance and thermal reflectance (which is the reflectance at one temperature divided by that at another; in this case that of the superconducting state divided by the normal state) in far-infrared range ( $0-40 \text{ cm}^{-1}$ ) are shown in Fig. 2.3 for a superconductor with an energy gap,  $2\Delta$  of width  $3.52 k_B T_c$ , and a dc-conductivity ( $\rho_{dc} = 2$  micro.ohm.cm) and a superconducting transition temperature ( $T_c = 1.6$  K) as parameters. As can be seen in this Figure, the superconducting state has higher reflectance than the normal state. Also in this Figure, the opening of the energy gap is noticeable as a peak in the thermal reflectance ( $R_S/R_N$ ).



## 2.3 Unconventional superconductors

Unconventional superconductors are materials that display superconductivity but that do not obey the BCS theory. The first unconventional organic superconductor  $(\text{TMTSF})_2\text{PF}_6$  (where TMTSF is tetramethyltetraselenafulvalene), was discovered by Jerome and Bechgaard in 1979 [5].

A series of BETS [bis(ethylenedithio)tetraselenafulvalene]-based molecular conductors with magnetic anions are unconventional superconductors that have provided ideal systems to study the competition between magnetism and electric conduction in organic conductors. In these systems, localized magnetic moments are known as insulating layers and electric conduction is dominated by  $\pi$ -electrons in BETS conducting layers. The strong interaction between the magnetic moments and the conduction  $\pi$ -electrons ( $\pi$ -d interaction) causes some fascinating phenomena such as a metal-insulator transition, or metal-superconductor-insulator transition [15].

### 2.3.1 Electronic Structure and Optical Properties of Unconventional Superconductors

As for ordinary metals, the electronic properties of organic charge-transfer salts are determined by the quasiparticles at the Fermi surface (FS). The energy-band structures for both the quasi-1D  $(\text{TMTSF})_2\text{X}$  and the quasi-2D  $(\text{ET})_2\text{X}$  salts have been calculated using a tight-binding scheme with a few simplifications. The calculations are based on the assumption that the intramolecular interactions are much stronger than the interactions between adjacent molecules in order to reduce the complexity of the problem enormously [16]. In a first step,  $\sigma$ - and  $\pi$ -molecular orbitals are constructed using linear combinations of atomic s- and p-orbitals of the constituent atoms. In the molecular-orbital (MO) approximation, the electrons (holes) are assumed to be spread over the whole molecule and only those electrons (holes) near the Fermi surface in the highest occupied (HOMO) and lowest unoccupied molecular orbitals (LUMO) are taken into account. The overlap between molecular orbitals of adjacent molecules causes the corresponding  $\pi$ -electrons (holes) to become delocalized [5], [15].

Infrared reflectance or conductivity spectra can provide important information on band parameters for metals, such as the effective mass, the band width, and the collision time of the carriers



[17]. By using polarized light, one can elucidate the anisotropy in the properties with respect to the orientation of the crystal axes. That is, the reflectance spectra show a distinct difference when the polarization is parallel or perpendicular to the conducting direction. The reflectance spectra of the ET salts can be analyzed in terms of a Drude model [4].

Through a study of reflectance spectra for various  $(\text{ET})_2\text{X}$  salts, one can calculate these optical properties. For instance, for  $\beta$  - $(\text{ET})_2\text{I}_3$ , the conductivity spectra converted from the reflection spectra exhibit a peak at  $2000 \text{ cm}^{-1}$  accompanied by a broad intraband Drude-like feature. For the light polarized along one particular direction, the conductivity peak is found but not for that perpendicular to it (Fig. 2.4). Thus it must be related to the molecular stacking structure, in particular, to the dimerization. The conductivity peak is attributed to the Electron-Molecular Vibration (EMV) coupling (that is described later) which causes absorption at the frequencies of the total symmetric intramolecular vibrations.

To separate intraband and interband transitions, the reflectance spectra have been analyzed by the following Drude-Lorentz model

$$\epsilon(\omega) = \epsilon_c - \frac{\omega_p^2}{\omega(\omega + i\gamma)} - \sum_j \frac{\Omega_{pj}^2}{(\omega - \omega_j)^2 - i\Gamma_j\omega} ,$$

where  $\epsilon_c$  is the frequency-independent dielectric constant,  $\omega_p$  and  $\gamma$  are the plasma frequency and the relaxation rate of the charge carriers, and  $\omega_j$ ,  $\Gamma_j$  and  $\Omega_{pj}$  are the resonance frequency, damping frequency and oscillator strength respectively of the Lorentz oscillations simulating the interband transitions and the vibrational structures [4], [18].

In a metal as the temperature decreases, the resistivity decreases as a result of which the conductivity increases. Higher conductivity results in higher reflectance *i.e.* this can also be noticed from the Hagen-Rubens equation in the low frequency region (See chapter 4 for more details). In the superconducting state, unit reflectance is expected below the superconducting energy gap,  $2\Delta$ . Substituting the reflectance in the Kramers-Kronig equations, the real and imaginary parts of the optical conductivity can be obtained. The dc-conductivity becomes infinite in the superconducting state and shorts out all parallel channels of conductivity. On the other hand, infrared techniques can measure the optical conductivity of the quasiparticles below  $T_c$ . That is, the optical conductivity is expected to exhibit a zero frequency delta function peak, followed by a gap up to  $2\Delta$ , which fills



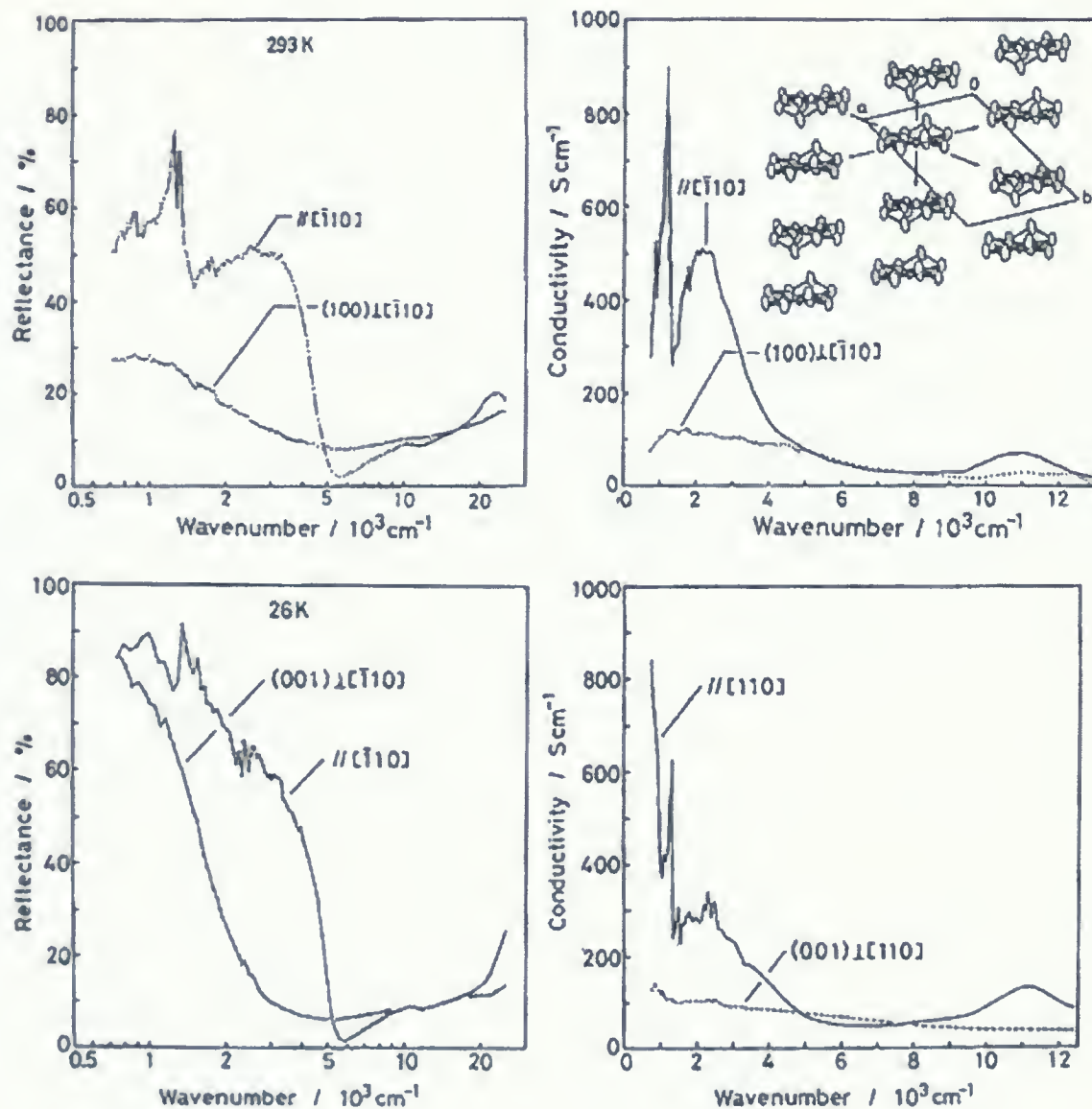


Figure 2.4: Reflectance and conductivity spectra for  $\beta$ -(ET)<sub>2</sub>I<sub>3</sub> at 293 K and 26 K [4].





in as the temperature increases from zero. Thus, optical methods are used to study and determine the energy gap, the spectrum of excitations and superconducting penetration depth tensor [?].

The BCS energy gap of low  $T_c$  superconductors is expected to occur at low frequencies according to:

$$2\Delta = 3.53k_B T_c = 2.45\text{cm}^{-1}T_c ,$$

where  $k_B$  is the boltzmann constant and  $T_c$  is the transition temperature. The infrared spectra of unconventional superconductors typically show the lack of an energy gap at  $2\Delta$  (which is the BCS superconducting energy gap) [?]. No previous work has been done on the optical properties of  $\kappa$ -(BETS)<sub>2</sub>FeBr<sub>4</sub> organic superconductor in the far-infrared region mainly due to the low frequency range, low  $T_c$  and the fragility of the samples. Thermal reflectance measurements at low frequencies and temperatures have been carried out on these samples in this thesis to investigate the effect of the SC and AF on the electromagnetic absorption. The results show that there could be increased reflectance below  $10\text{ cm}^{-1}$  that may be due to the opening of the superconducting gap which is not consistent with the BCS energy gap ( $2.5\text{ cm}^{-1}$ ) indicating that for this unconventional superconductor,  $2\Delta/k_B T_c > 3.53$ .

### 2.3.2 Electron-phonon coupling

Infrared reflectivity measurements can also be used to obtain information on the electron-phonon interaction. In molecular crystals, the coupling between the conduction electrons and the phonons is of two kinds. One kind of interaction, the electron-molecular-vibration (EMV) coupling, involves the intramolecular vibrations which are characteristic of the molecular structure. Another kind is the electron-intermolecular-vibration coupling which refers to the interaction of the charge carriers with motions of almost rigid molecules around their equilibrium positions and orientations (translational and librational modes) [5].

*Electron-molecular-vibration coupling:* The electrons in the highest occupied molecular orbitals (HOMO) of the TTF molecule and its derivatives couple strongly to the totally symmetric molecular vibrations via the modulation of the HOMO energy,  $E_{HOMO}$ , by the atomic displacements. For the ET molecule, the modes with the strongest coupling constants are those involving the central carbon



and sulfur atoms. The linear EMV coupling constant  $g_i$  for mode  $i$  is defined as:

$$g_i = \frac{1}{h\nu_i} \frac{\partial E_{HOMO}}{\partial Q_i} ,$$

where  $Q_i$  is an intramolecular normal coordinate and  $\nu_i$  the mode frequency. Then one can calculate the effective electron-intramolecular-phonon coupling constant  $\lambda_i$  using the following equation:

$$\lambda_i = 2g_i^2 h\nu_i N(E_F) ,$$

where  $N(E_F)$  is the density of states at the Fermi level.

In the ET molecules, the frequencies of these C=C stretching and ring-breathing modes are  $\nu_2 = 1465 \text{ cm}^{-1}$  ( $g_2 = 0.165$ ),  $\nu_3 = 1427 \text{ cm}^{-1}$  ( $g_3 = 0.746$ ) and  $\nu_9 = 508 \text{ cm}^{-1}$  ( $g_9 = 0.476$ ), where the calculated coupling constants are given in the brackets. Despite these sizable coupling constants, several studies - especially those of the mass isotope shifts on  $T_c$  for the ET salts [19]- indicate that the EMV coupling seems to play only a minor role in mediating the attractive electron-electron interaction [5].

*Electron-intermolecular-vibration coupling:* While much experimental data are available on the EMV coupling, relatively little is known about the coupling of the charge carriers to the low-lying intermolecular phonons [5]. The modulation of the charge-transfer integrals  $t_{eff}$  between neighboring molecules during their translational or librational motions provides this interaction. Within the Eliashberg theory, the dimensionless electron-intermolecular-phonon coupling constant  $\lambda$  can be calculated using:

$$\lambda_{ph} = 2 \int \frac{\alpha(\omega)^2}{\omega} F(\omega) d\omega ,$$

where  $\alpha(\omega)$  is the electron-phonon-coupling constant,  $\omega$  the phonon frequency and  $F(\omega)$  the phonon density of states. The Eliashberg function  $\alpha(\omega)^2 F(\omega)$  can be derived from tunneling characteristics of strong-coupling superconductors [5]. Some of the frequencies of the intermolecular modes have been determined through Raman and far-infrared measurements. More recent studies including inelastic neutron and Raman-scattering have focused on investigation of the role of intermolecular phonons for superconductivity [20]. These experiments resulted in quite sizable superconductivity-induced phonon-renormalization effects which shows a significant coupling of the superconducting charge carriers to the intermolecular phonons and suggests an important role of these modes in the



pairing interaction [5].



## Chapter 3

# Experimental setup

### 3.1 Martin-Puplett Interferometer:

The Martin-Puplett Interferometer (MPI) is a modern polarizing spectrometer and has several advantages over the Michelson type where the main one is that it allows lower frequencies to be reached. Other advantages include: 1) Two outputs allow for a differential measurement which makes the removal of intensity fluctuations possible. 2) For a linearly polarized source (like synchrotron radiation), nearly no intensity is lost [21], [22]. The data gathered from this interferometer (ScienceTech, Model No. SPS-200) is called an interferogram which is a plot of intensity versus mirror position. The power spectrum can be calculated from the interferogram by taking the Fourier Transform [23].

Figure 3.1 shows the scheme of this interferometer which uses a Mercury-Xenon (Hg-Xe) light source. After reflection of the source light from mirrors M1, M2 and M3 in turn, the light passes through the P1 polarizer which polarizes the light horizontally. Then upon interacting with the 45° polarizing beam splitter, the polarized light splits into two; half of the light transmits and the other half reflects. These two beams hit the two roof mirrors (RM1, RM2) and they reflect back with a 90° rotation of the polarization to the beam splitter. At the beamsplitter the initially transmitted beam is reflected, while the initially reflected beam is transmitted, and thus the two beams recombine. The resulting beam reflects from mirrors M4 and M5 and then passes through a polarizing chopper (polarization modulator C2) to reduce the background noise before it exits the interferometer [24], [25], [26].





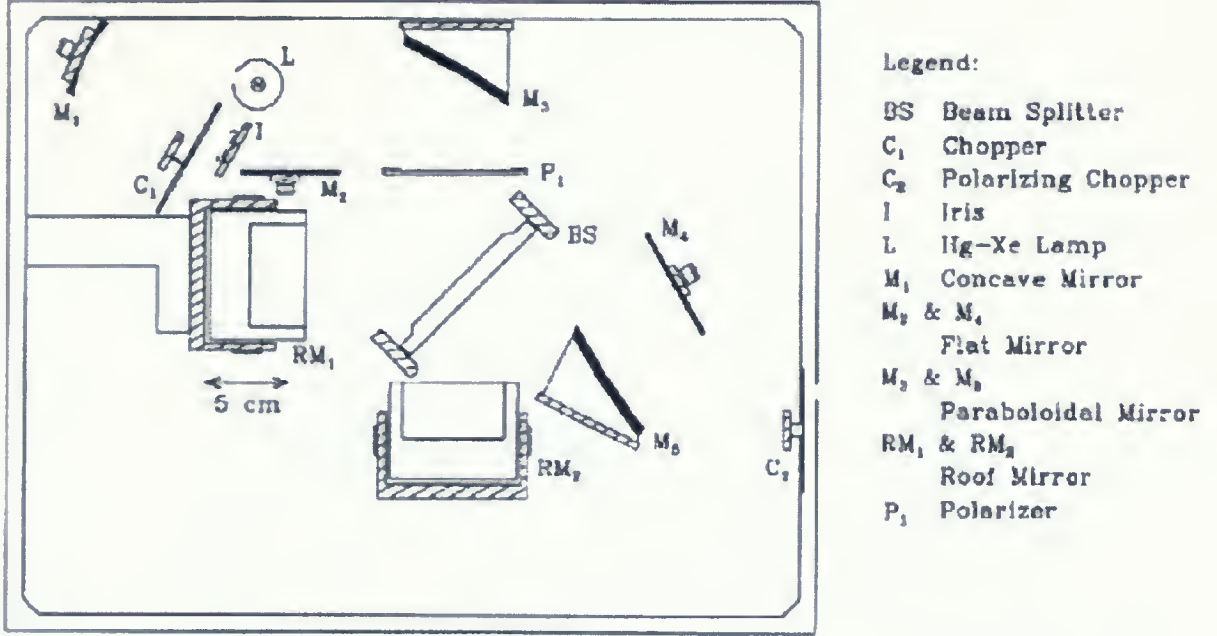


Figure 3.1: Martin-Puplett Interferometer [22].

### 3.2 The Helium-3 Cryostat:

Using a  $^3\text{He}$  cryostat for this setup (Infrared Laboratories Model No. HDL-10 Dual  $^3\text{He}$ ) is very advantageous since the experiment can be conducted at low temperatures (0.5 K). As it is shown in Figure 3.2, the light enters the  $^3\text{He}$  cryostat through one of two light pipes and hits either the sample or reference mirror which reflect the light to the Bolometer detector.

On the other end of this cylindrical cryostat (Figure 3.3), there is a liquid  $^4\text{He}$  container surrounded by vacuum, liquid  $\text{N}_2$  and vacuum layers respectively [27], [28]. There are also two  $^3\text{He}$  gas cylindrical tanks attached to the side of the cryostat [29].

Liquid helium in the  $^4\text{He}$  container has a boiling point of 4.2 K. In order to reduce the temperature, one has to pump on the liquid helium bath to reduce the pressure on top of the container which



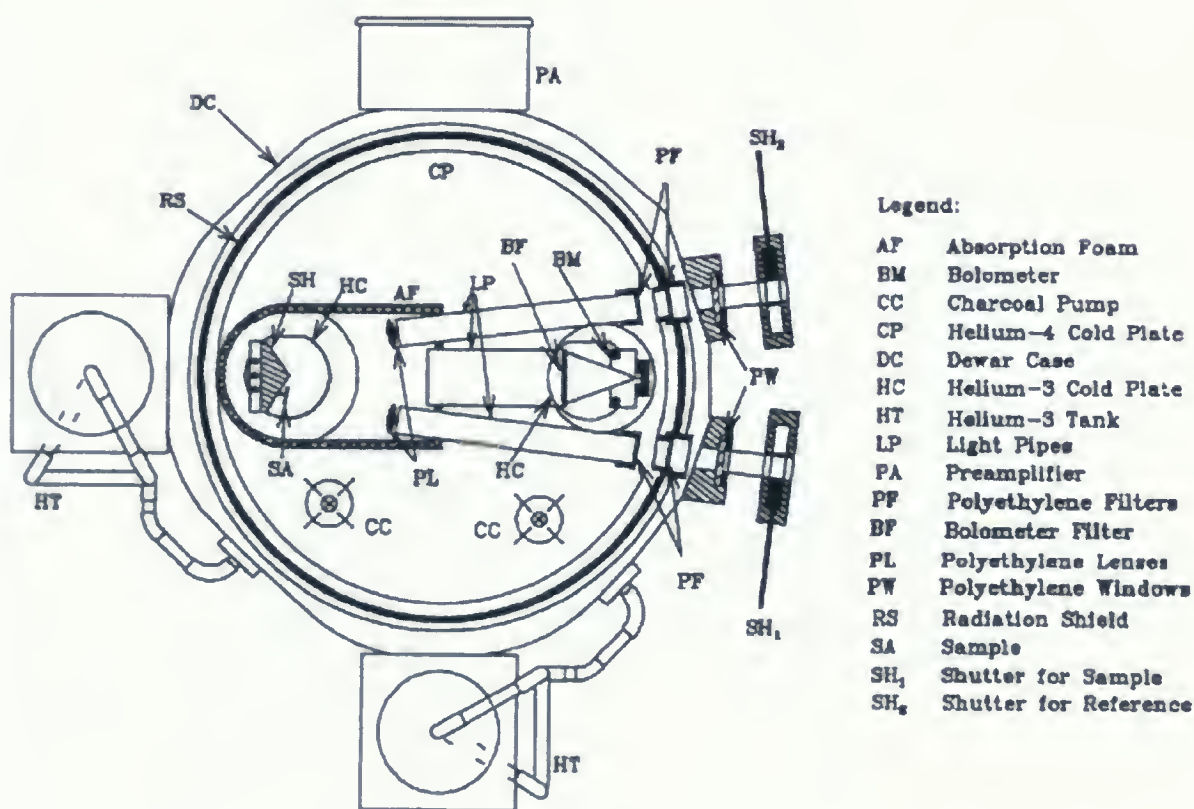


Figure 3.2: The Helium-3 Cryostat [21]. Note that the sample stage which houses the sample and a reference mirror, and the bolometer stage which houses the detector are separate so that the experiment can be carried out in the range of 0.4 K - 90 K.







causes the temperature of the  $^4\text{He}$  to drop to  $\sim 2$  K. At this point the temperature is less than the  $^3\text{He}$  boiling point (3.2 K) so  $^3\text{He}$  gas gets liquefied onto the  $^3\text{He}$  cold plate which is at this point still thermally connected to the  $^4\text{He}$  bath. The  $^3\text{He}$  cold plate is then thermally disconnected from the  $^4\text{He}$  bath and with a similar procedure of reducing the pressure over the liquid  $^3\text{He}$  bath using a charcoal adsorption pump, the temperature drops to almost 0.4 K.

The details of the experimental procedure are as follows: There are four switches at the bottom of the cryostat (charcoal pump heat and refrigerator switches) to connect or disconnect the sample and bolometer stages and the charcoal pumps from the  $^4\text{He}$  cold plate. Initially, the refrigerator switches are closed to connect the sample and the bolometer stages to the  $^4\text{He}$  bath which is at almost 4 K. The  $^3\text{He}$  tank valves are open and the charcoal pump heat switches are closed to adsorb the  $^3\text{He}$  gas onto the charcoal. After coming to thermal equilibration, one closes the  $^3\text{He}$  tank valves to ensure that the gas does not go back into the tank and disconnects the charcoal pump heat switches from the  $^4\text{He}$  cold plate. The pressure over the  $^4\text{He}$  bath is decreased using a rotary pump. This makes the temperature drop below 3 K at which point the  $^3\text{He}$  gas liquifies onto the  $^3\text{He}$  cold plate. Note that during the  $^4\text{He}$  pump down procedure, a certain amount of voltage is applied to the charcoal pump heaters in order to drive the adsorbed  $^3\text{He}$  from the charcoal and get condensed onto the cold plate. At almost 2 K, the refrigerator switches have to be disconnected which thermally isolates the  $^4\text{He}$  bath from the  $^3\text{He}$  cold plate. At this stage, the liquid  $^4\text{He}$  pump down is over and by connecting the charcoal pump heat switches the  $^3\text{He}$  gas above the  $^3\text{He}$  bath gets adsorbed onto the charcoal lowering the pressure above the liquid  $^3\text{He}$  bath and causes the temperature to drop to 0.4 K.

The bolometer stage has to be kept at 0.4 K to work properly but the temperature of the sample stage may vary depending on the experiment. By connecting the sample stage refrigerator switch, the sample stage becomes thermally connected to the  $^4\text{He}$  bath which is at 4.2 K. To reach higher temperatures the connection with the  $^4\text{He}$  bath is broken and a heater is used to fix the temperature at a required point. After approximately 24 hours, the system runs out of liquid  $^4\text{He}$ . As the cryostat warms up the  $^3\text{He}$  gas goes back to the cylindrical  $^3\text{He}$  tanks [21], [30], [31].





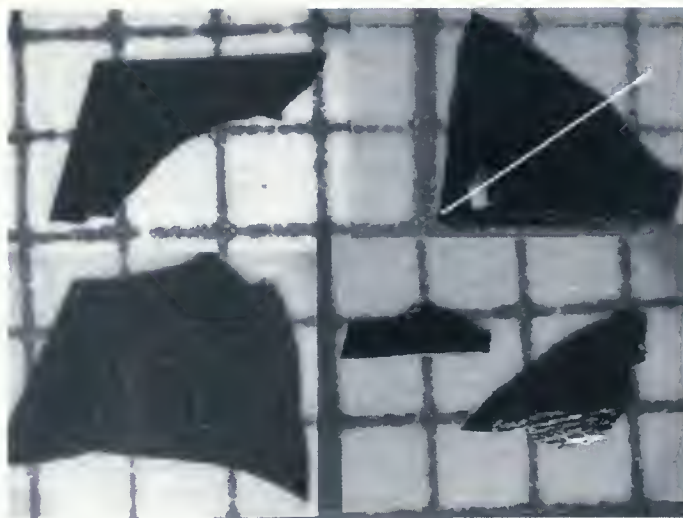


Figure 3.4:  $\kappa$ -(BETS) $_2$ FeBr $_4$  sample pieces with the dimension of each block on the grid 1.27 mm.

### 3.3 Sample preparation:

The rhombus shaped  $\kappa$ -(BETS) $_2$ FeBr $_4$  samples with orthorhombic structure (Fig. 3.4) were received from Dr. Tanatar, Institute of Molecular Science, Okazaki, Japan.

Unfortunately, the samples of average dimensions 2 mm  $\times$  3 mm were broken pieces with just one or two straight edge(s) rather than having the full shape of a rhombus. Therefore, it was necessary to determine the  $a$ -axis (easy axis), which falls along the long diagonal of the rhombus, by a means other than by sight.

Initially, some effort was made to find the sample orientation through a polarizing microscope (Cooke, Model No. M703031 ) but no changes were observed upon rotation of the polarizer. After that, digital pictures were taken of the tiny samples and enlarged. The small and large angles of the rhombus were determined to be 74° and 106° respectively.

One of the samples (with the triangular shape) had enough straight edges that the easy axis could be determined via identification of the diagonal. It was epoxied to a very smooth post (polished to 1  $\mu$ ) which is screwed into the sample holder and inserted into the Helium-3 cryostat. The sample was oriented with the easy axis vertically. A far infrared polarizer was used in front of the Bolometer



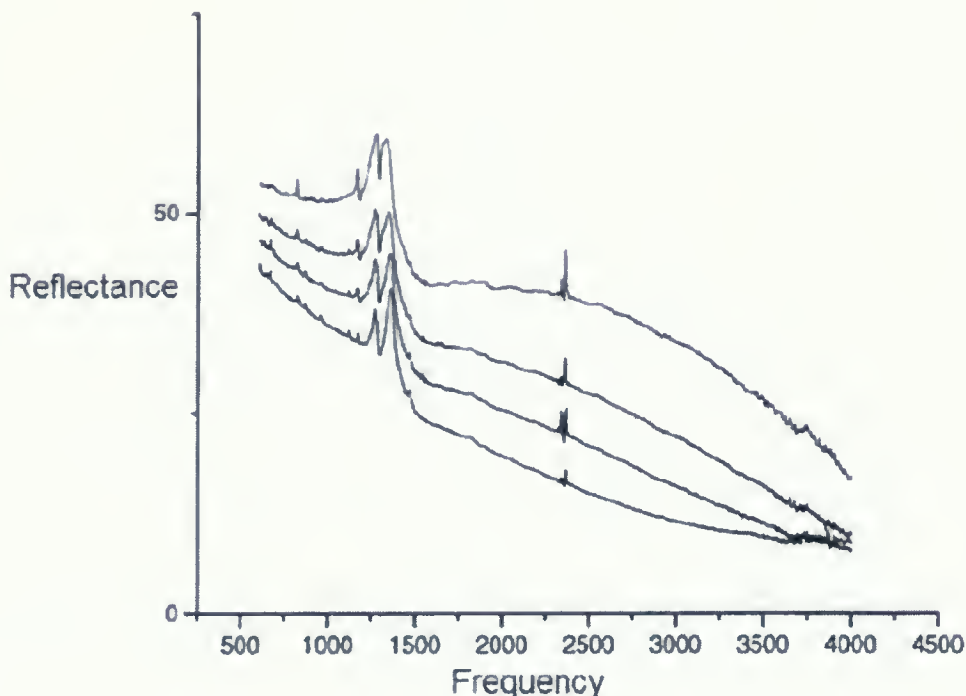


Figure 3.5: Plot of Reflectance versus Frequency for different orientations measured on an infrared microscope by M. Tanatar The top curve is along the easy axis ( $a$ -axis).

stage and data (interferogram and power spectrum) was obtained at different temperatures (0.5 K and 2.5 K). Unfortunately, the signal was very small due to the small size of the sample and the use of the polarizer and thus the results were very noisy.

Then another set of experiments was carried out without the polarizer in two different frequency ranges ( $0\text{--}40\text{ cm}^{-1}$  and  $30\text{--}200\text{ cm}^{-1}$ ) using black poly on crystalline quartz plus fluorogold and diamond powder on crystalline quartz filters respectively on the detector stage. The signal improved somewhat but the data was still too noisy to see any reliable structure.

Making a mosaic out of the sample pieces was the next option to increase the signal. After a meeting with Dr. Tanatar, he demonstrated a plot of reflectance versus frequency obtained using an infrared microscope on  $\kappa\text{-(BETS)}_2\text{FeBr}_4$  along different directions relative to the  $a$ -axis as shown in Fig. 3.5. This data exhibits anisotropy with the highest curve along the easy axis. So, in order to increase the signal significantly, the pieces had to be placed beside each other with the same



*a*-axis orientation. Because of the odd shapes that these samples had, it was not possible to create a mosaic without having a huge gap or significant overlap between pieces. Extensive overlap was undesirable due to the fact that we only had available the crystal pieces shown in Fig. 3.4.

Eventually, it was decided to place each sample on a separate post and to determine the exact *a*-axis orientation individually. Then the posts would be placed in close vicinity to each other on a sample holder block so that the samples have the same easy axis direction. The block could then be placed into the Helium-3 cryostat and data would be gathered at low frequencies at different temperatures (0.5 K, 1.4 K, 1.9 K, 2.8 K, 10 K, 25 K, 30 K, 35 K, 40 K, 60 K and 80 K). This will be discussed in chapter 4.

### 3.4 Thermal Reflectance

The output result of the experiment is the power spectrum (a plot of intensity versus wave number) which is a Fourier transform of the interferogram (a plot of intensity versus the mirror position). In order to eliminate environmental effects from the sample data, a ratio of the sample power spectrum divided by the reference power spectrum is taken (reference is a mirror with almost the same area as that of the sample). This ratio is called the reflectance (not absolute reflectance) for a specific temperature. The quotient of the reflectance at one temperature ( $T_1$ ) divided by the reflectance at another temperature ( $T_2$ ) is called the thermal reflectance which is used to compare the characteristics of the sample at different temperatures.



## Chapter 4

## Results

### 4.1 Optical results for the $\kappa$ -(BETS)<sub>2</sub>FeBr<sub>4</sub> samples

The largest surface of the plate shaped samples of  $\kappa$ -(BETS)<sub>2</sub>FeBr<sub>4</sub> is the  $ac$ -plane. Since the infrared microscope work discussed in Chapter 3 observed anisotropy between the  $a$ - and  $c$ -axes, there was a need to determine these two main orientations in these samples. In order to find the easy axis ( $a$ -axis) and the perpendicular  $c$ -axis, a Bruker interferometer Model No. IFS 66v/S (a type of Michelson interferometer in the Far-Mid infrared range) and a rotational mount with a Far-Mid infrared polarizer (InfraSpecs Model No. P03) were used.

Each sample was mounted separately on a copper post which was screwed into a sample holder which was placed within the cold-finger cryostat attached to the Bruker interferometer. A Mid-Infrared (Globar) source of light with the KBr beamsplitter and a Mercury Cadmium Telluride detector (InfraRed Associates, Model No. INSB-1.0) were used. By rotating the polarizer every 5 degrees and by comparing the intensity obtained from the sample path with the reference path, plots of interferogram maximum intensity versus the angle (Fig. 4.1) were obtained for the three largest samples. Fig. 4.1 shows that intensity is behaving sinusoidally with respect to angle. This Figure may be interpreted such that for each maximum, the polarization was along the  $a$ -axis and for each minimum it was along the  $c$ -axis. Note that as expected the maximum and the minimum are separated by 90° degrees. The orientation of the larger triangular sample was known from the geometry (with two straight edges of a rhombus) and it was used to test the procedure successfully.





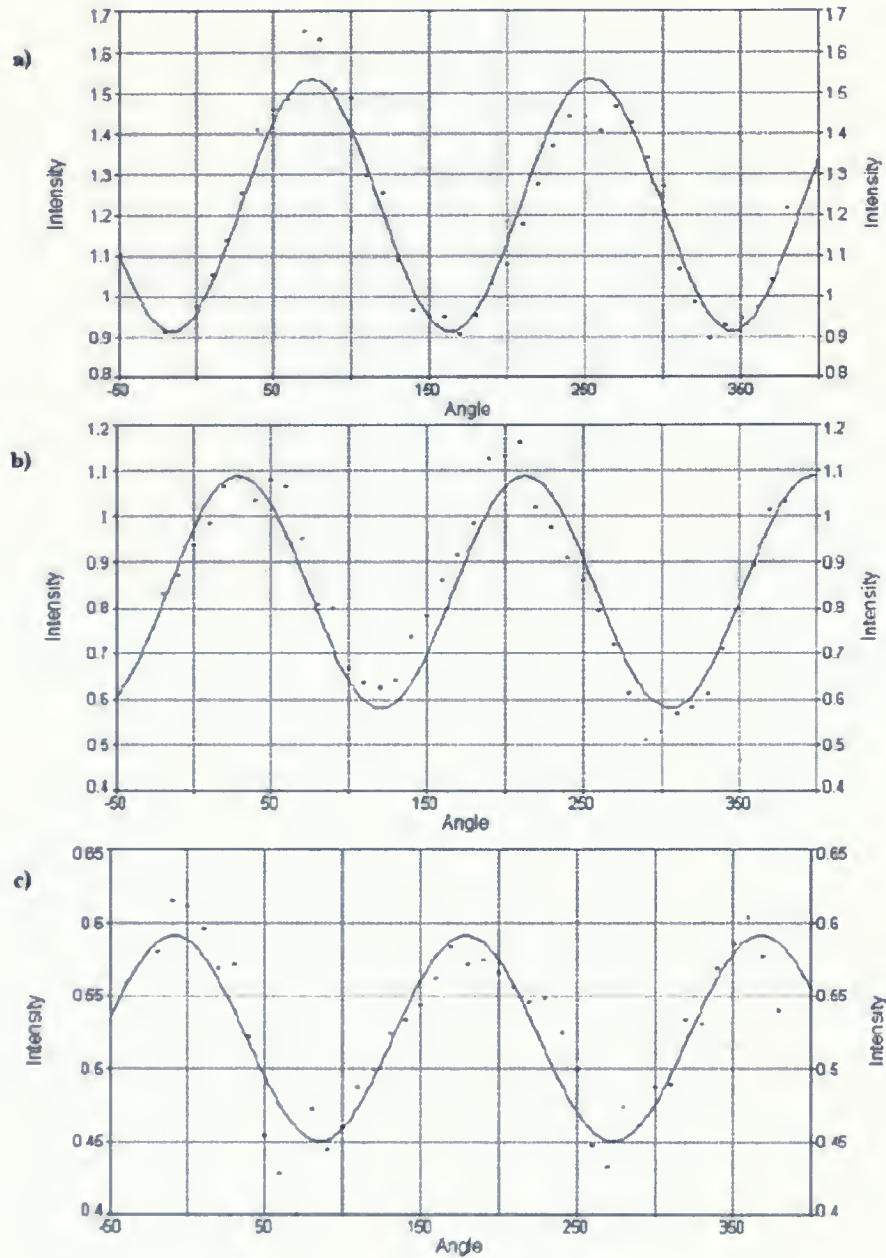


Figure 4.1: Sinusoidal plots of intensity versus angle to find the easy axis including  $y = a + b\sin(2\pi X/d + c)$  as the fitting equation and parameters a) Corresponds to the trapezium sample with  $a=1.225$ ,  $b=0.310$ ,  $c=5.263$ ,  $d=179.934$ . b) Corresponds to the larger triangular sample with  $a=0.8345$ ,  $b=0.2544$ ,  $c=0.591$ ,  $d=184.661$ . c) Corresponds to the small triangular sample with  $a=0.521$ ,  $b=0.703$ ,  $c=1.870$ ,  $d=188.523$ .





Figure 4.2:  $\kappa$ -(BETS) $_2$ FeBr $_4$  samples on the copper block showing three samples oriented with the easy axis vertical on the left and the reference mirror on the right.

By using these plots, all three of the samples were aligned with their easy axes vertical and placed on a copper block in order to be mounted in the  $^3\text{He}$  cryostat (Fig. 4.2 ).<sup>1</sup>

In order to perform an experiment at low temperatures and in the very far infrared frequency range ( $0\text{--}60\text{ cm}^{-1}$ ), a Sciencetech Martin-Puplett Interferometer connected to the Infrared Laboratories  $^3\text{He}$  cryostat play the main role (Figures 3.2 and 3.3). To prepare for the experiment: 1) The copper block holding three aligned samples was placed on the sample stage in the  $^3\text{He}$  cryostat, 2) a vertical polarizer was placed in front of the bolometer (detector) to polarize the light along the easy axis, and 3) black polypropylene on crystalline quartz and fluorogold filters were placed in front of the bolometer while black polypropylene on crystalline quartz filters were mounted within the inner and outer light pipes to transmit the low frequency range of the Mercury-Xenon light source.

<sup>1</sup>It was planned to make an oriented mosaic out of these samples on one post but since the samples were so small, thin and fragile, after finding the  $a$ -axis of each separately, it would be almost impossible to remove them from their individual posts. Furthermore, small gaps between crystals and optical misalignment would be inevitable. Thus, the idea came along to align these individual sample posts separately on a copper block holder.



A set of experiments was performed on the  $\kappa$ -(BETS)<sub>2</sub>FeBr<sub>4</sub> samples along the easy axis at different temperatures. The bolometer temperature was kept at 0.380 K in order for the detector to work properly, while the sample stage temperature was varying. Several sets of data were gathered when the samples were at the following temperatures: 0.5 K (sample in both superconducting (SC) and antiferromagnetic (AF) states), 1.4 K (above SC state and in the AF state), 1.9 K (above SC state and in the partially developed AF state), and 2.8 K (normal state which is above the SC and AF states).

The resulting thermal reflectance ratios of different temperatures (which represent the AF and/or SC states) are plotted in Fig. 4.3 showing five situations. The error bars are also shown in this Figure using the standard deviation and error formula of a ratio (e.g. Thermal reflectance =  $R(T_1)/R(T_2)$  where  $T_1$  and  $T_2$  are two different temperatures and  $R$  represents the reflectance). Fig. 4.3 (a) shows the ratio of the reflectance in both the SC and AF states (since at 0.5 K the sample has undergone the AF transition ( $T_N = 2.5$  K) and the SC transition ( $T_c = 1.1$  K)) to that at 2.8 K in the normal state. In this plot, since there can be seen a rising in the thermal reflectance (where the arrow is pointing) at low frequencies (below  $15 \text{ cm}^{-1}$ ) the reflectance in the SC and AF states is higher than that in the normal state.

Figures 4.3 (b) and (c) contain information about the AF state since at both temperatures the AF is partially developed. As the arrow illustrates, there is a dip-like feature in this plot at low frequencies which indicates that the reflectance in the AF state is lower than in the normal state. Fig. 4.3 (d) may provide the best glimpse of the effect of superconductivity on the reflectance since the AF exists at both 0.5 K and 1.4 K and its effects may cancel out somewhat after the division. Again, a rising thermal reflectance is observed at the lowest frequencies indicating that the reflectance in the SC state is higher than that in the normal state. In Fig. 4.3 (e) where both temperatures represent the partially developed AF state,  $R(1.4 \text{ K})$  and  $R(1.9 \text{ K})$  are almost the same except that the AF may be slightly more developed at 1.4 K than at 1.9 K and thus we see very little change in the thermal reflectance.



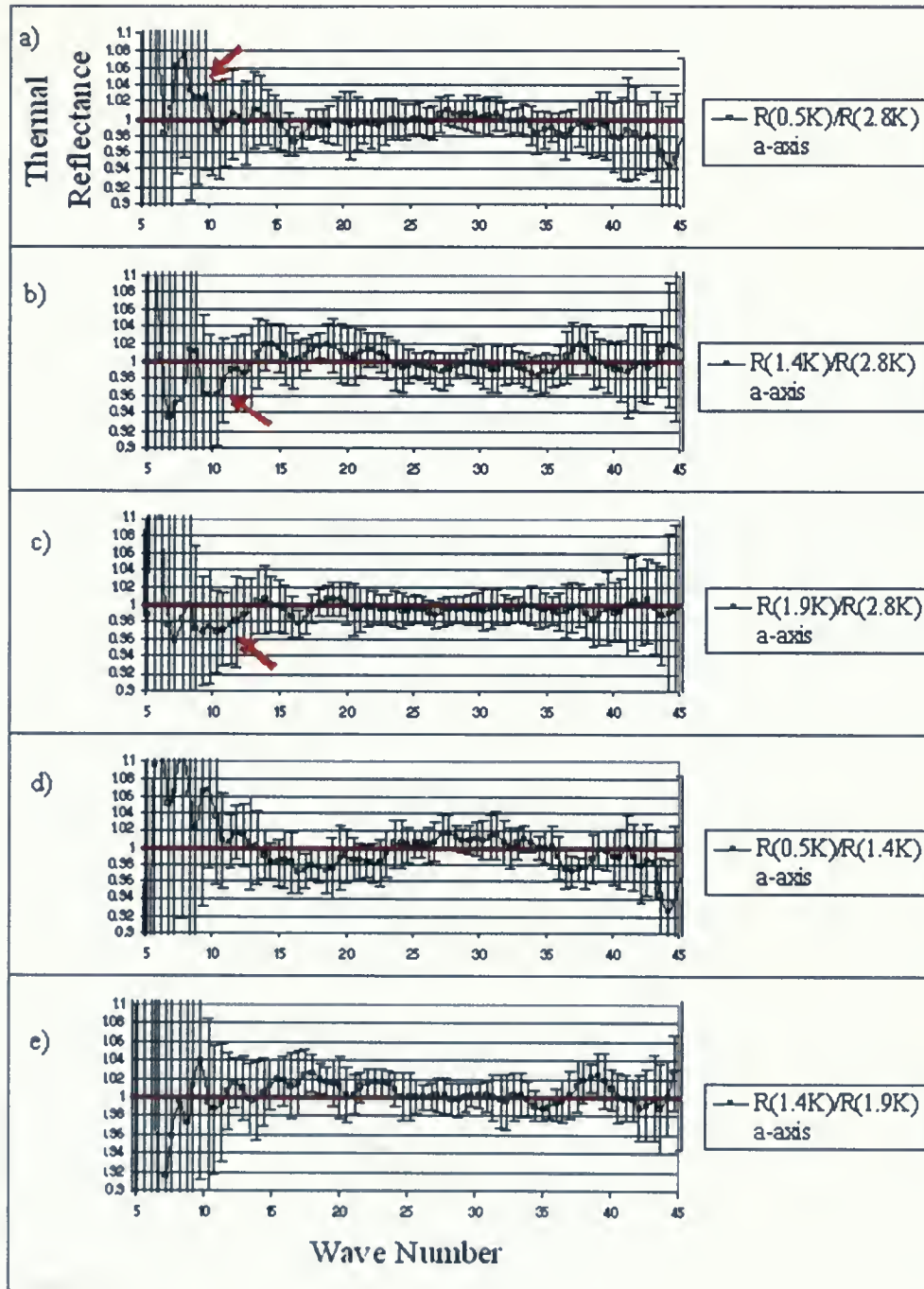


Figure 4.3: Thermal reflectance of the three samples versus wave number along the  $a$ -axis in five different situations.





Upon comparing those plots including the SC state (Figures 4.3 (a) and (d)) with the rest not in the SC state, it might be concluded that the reflectance in the SC state increases at low frequencies ( $10 \text{ cm}^{-1}$  and below) which may indicate the energy scale of the superconducting energy gap. There is an overall depression at low frequencies (approximately below  $15 \text{ cm}^{-1}$ ) in Figures 4.3 (b) and (c) which may be significant for the antiferromagnetic state perhaps to the AF gap. Also the small dip-like feature appearing in Figures 4.3 (a), (b) and (c) around  $17 \text{ cm}^{-1}$  could be due to the antiferromagnetic ordering. It is helpful to compare these results with other samples exhibiting SC and/or AF states. For instance  $\text{URu}_2\text{Si}_2$  becomes antiferromagnetic at  $T_N = 17.5 \text{ K}$  and there is a dip-like feature in its reflectance plot near  $42 \text{ cm}^{-1}$  at temperatures below  $T_N$  caused by an energy gap associated with the antiferromagnetic transition [32]. As another example,  $\text{Sr}_2\text{RuO}_4$  has a superconducting transition at  $T_c = 1.42 \text{ K}$  and its thermal reflectance plot ( $R_S/R_N$ ) shows a peak near  $9 \text{ cm}^{-1}$  which is attributed to be due to the formation of the SC energy gap [33].

A second experiment was performed on these three samples along their  $c$ -axis (perpendicular to the  $a$ -axis) by rotating the polarizer to the horizontal direction. Similar to Fig. 4.3, plots of thermal reflectance are shown in Fig. 4.4. Although in general there is an anisotropy between the  $a$ - and  $c$ -axis reflectance, the overall trends in the five plots of thermal reflectance in Fig. 4.4 are similar to those in Fig. 4.3. In other words, the features in Fig. 4.3 that were attributed as arising due to the SC and AF states also appear along the  $c$ -axis and thus there does not seem to be a significant difference in the low frequency, low temperature optical properties along the easy axis compared to the normal axis. In both Figures 4.3 and 4.4 the small sinusoidal dips and peaks are mainly due to incomplete cancelation of interference fringes. Also, note that in most cases where there is a small change in the thermal reflectance at low frequencies, a thermal reflectance of unity is still possible within the errorbars, and thus the results must be considered with this caveat in mind. These experiments were difficult and very time-consuming and unfortunately the error increases at low frequencies where changes in the reflectance might be expected to occur.

During the experiment in which light was polarized along the easy axis of the  $\kappa$ -(BETS) $_2\text{FeBr}_4$  samples, the temperature was also varied from 10 K to 80 K ( $T = 10 \text{ K}, 25 \text{ K}, 30 \text{ K}, 35 \text{ K}, 60 \text{ K}, 80$



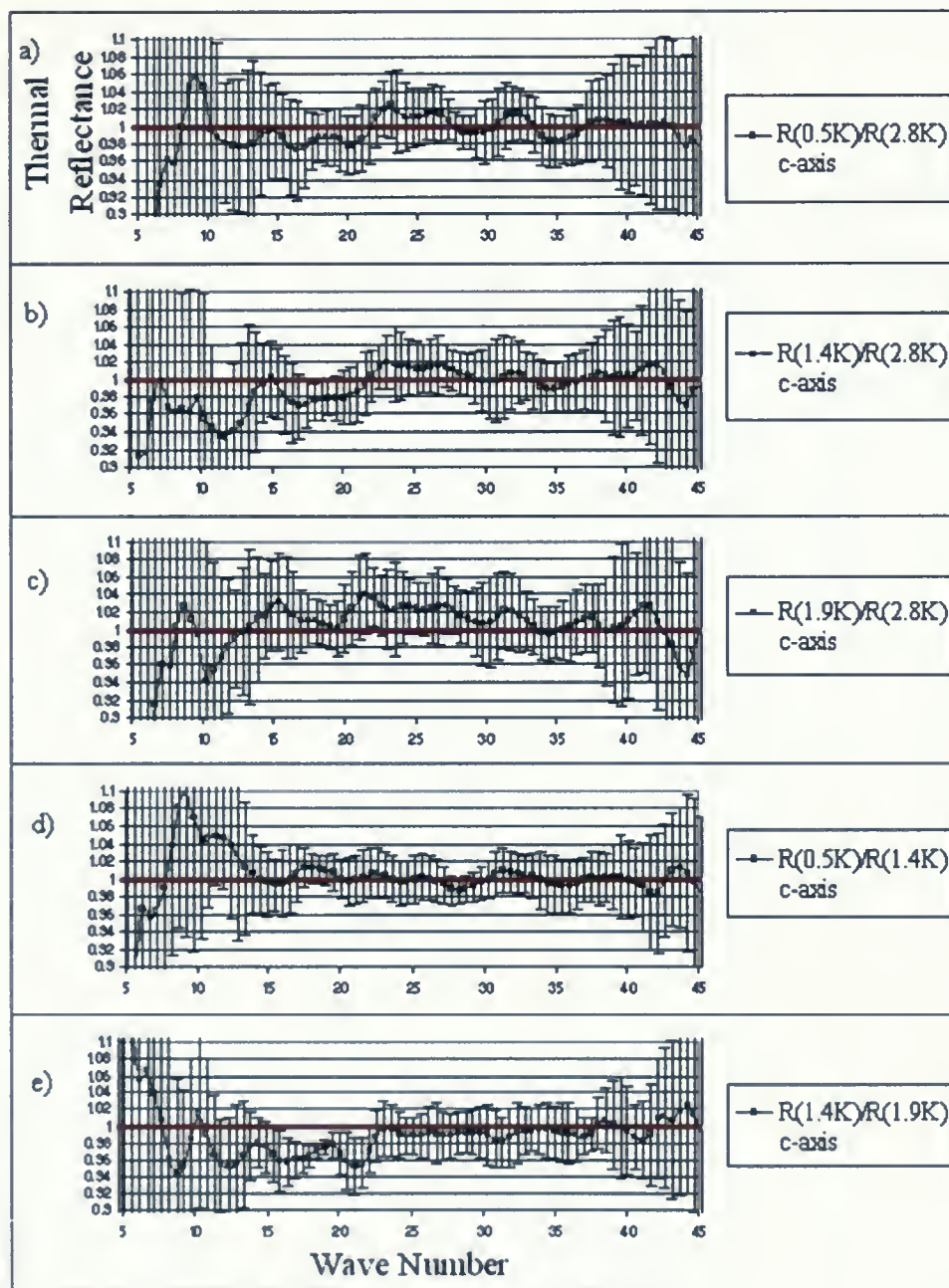


Figure 4.4: Thermal reflectance of the three samples versus wave number along the  $c$ -axis in five different situations.



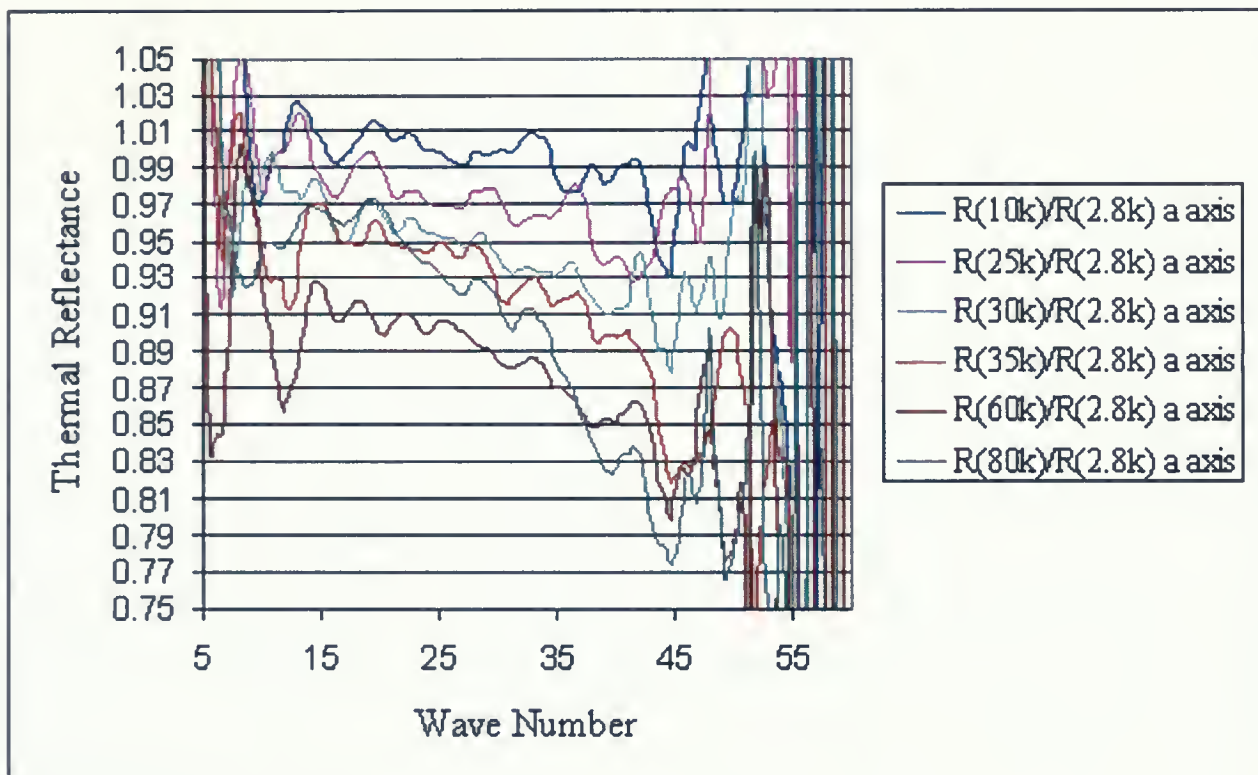


Figure 4.5: The thermal reflectance at six different temperatures along the  $a$ -axis.

K) in order to observe the temperature dependence of the thermal reflectivity along the  $a$ -axis with the onset of coherence below 60 K (coherent temperature). The reflectance at each of these higher temperatures was divided by the reflectance at 2.8 K which was chosen to be the base temperature. The results are shown in Fig. 4.5.

Along the  $c$ -axis higher temperature measurements were also performed ( $T = 25$  K, 30 K, 35 K, 40 K, 60 K) and each data set was divided by 2 K as the base temperature (Fig. 4.6).<sup>2</sup> Figures 4.5 and 4.6 show that the reflectivity decreases with increasing temperature, which was also expected from Fig. 1.5 which shows that the resistivity ( $\rho_{dc} = 1/\sigma_{dc}$ ) increases with increasing temperature to 60 K above which the resistivity decreases again. This phenomenon can be confirmed in Fig. 4.5,

<sup>2</sup>Along the  $c$ -axis, since the 2 K data sets were better than the 2.8 K data sets and the reflectance at these two temperatures is expected to be very similar, the base temperature was chosen to be 2 K.





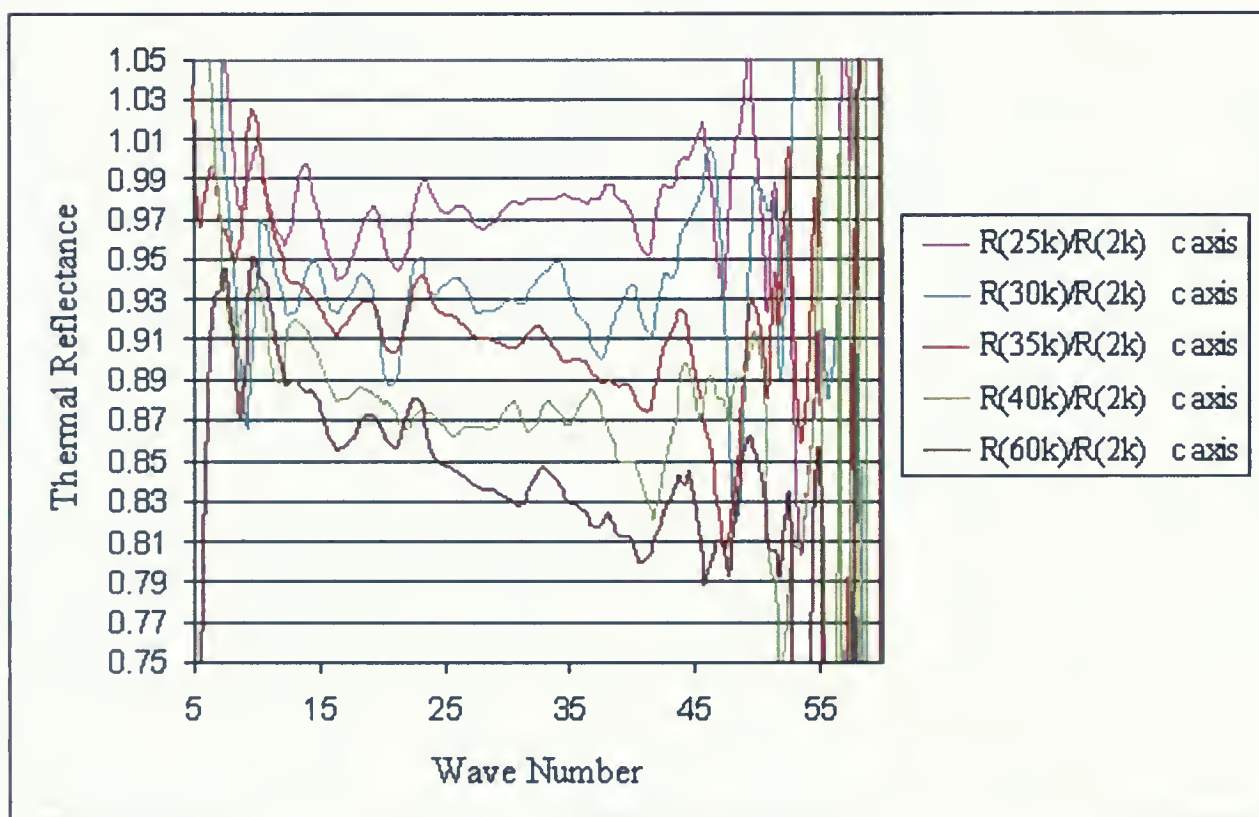


Figure 4.6: The thermal reflectance at five different temperatures along the *c*-axis.





where the reflectance at 80 K is higher than that at 60 K (The discussion in Section 4.2 concerning the Hagen-Rubens Reflectance shows that the low frequency free carrier reflectance decreases with decreasing dc-conductivity).

Little is known regarding the anisotropy in the transport and optical properties along the  $a$ - and  $c$ -axes. Fig. 4.7 shows the anisotropy in the thermal reflectance at four different temperatures. There seems to be a crossing point between the two thermal reflectance curves in each plot of Fig. 4.7 and with increasing temperature, this point moves to higher frequencies and the gap between the two curves at low frequencies increases. Consequently, since there is a noticeable difference ( $\sim 6$  percent) in the reflectance curves at 60 K at low frequencies, the anisotropy between the  $a$ - and  $c$ - axes is more evident.

It would be highly desirable to obtain absolute reflectance:

$$R_{\text{absolute}} = \frac{\text{sample reflectance}}{\text{reference reflectance}} \div \frac{\text{gold reflectance}}{\text{reference reflectance}} \times \text{Known reflectance on gold}$$

in order to obtain the optical conductivity through Kramers-Kronig analysis. However, due to the thinness and brittleness of samples and the fact that we could not obtain more samples than what we had available to us, we can likely only evaporate gold onto the samples once, thus all measurements need to be completed before this occurs. Due to time constraints it was not possible to make high frequency measurements and thus determination of absolute reflectance could not be carried out for this thesis. This aspect of the work will be continued by other members of the group, and thus it is anticipated that in the future the optical conductivity along the  $a$ - and  $c$ - axes will be obtained for  $\kappa$ -(BETS)<sub>2</sub>FeBr<sub>4</sub> from which the anisotropy in the transport properties can be evaluated.

## 4.2 Hagen-Rubens Calculation

The Drude reflectance at very low frequencies in metals ( $\omega \ll \gamma$  and also  $\omega \ll \sigma_{dc}/\epsilon_0$ ), becomes the Hagen-Rubens reflectance which shows that  $R$  is decreased from unity as  $(\omega^{1/2})$  in this region [18], [3].



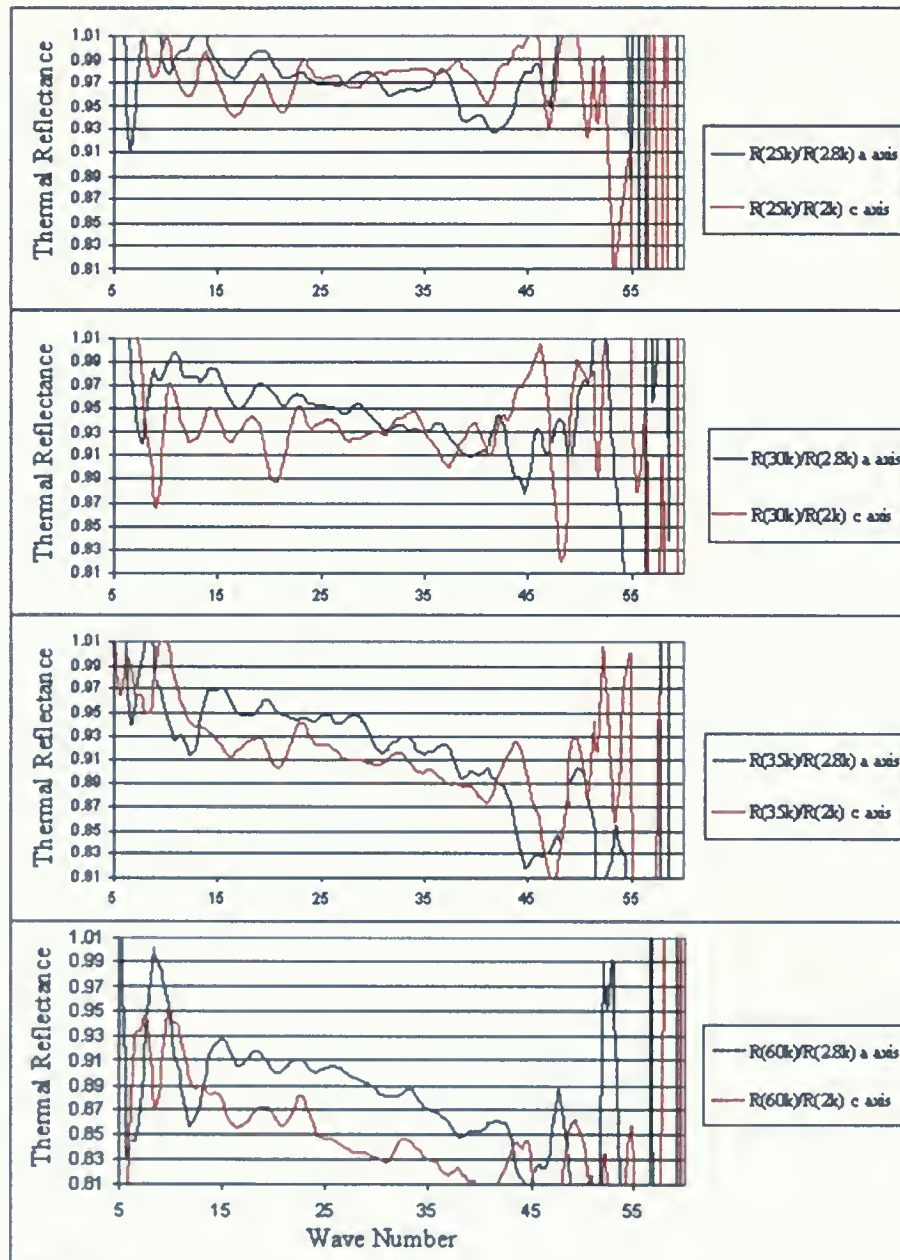


Figure 4.7: Comparison of the thermal reflectance curves along the *a*- and *c*-axes at four different temperatures.



$$R = 1 - 2\left(\frac{2\epsilon_0\omega}{\sigma_{dc}}\right)^{1/2} \quad (1)$$

In this equation, if the static conductivity ( $\sigma_{dc}$ ) is known then the frequency dependence of the reflectance would be determined.

The temperature dependent resistivity relative to that at room temperature has been measured by Fujiwara *et al.* (Fig. 1.5) for  $\kappa$ -(BETS)<sub>2</sub>FeBr<sub>4</sub>. Thus, since the room temperature resistivity is known [7] (the dc-conductivity at room temperature = 60 S cm<sup>-1</sup>), the resistivity and corresponding dc-conductivity ( $\sigma_{dc} = 1/\rho_{dc}$ ) at each temperature could be determined and the Hagen-Rubens reflectance (HR) calculated using equation 1. Note that the experimental resistivity values used correspond to the *ac*-plane. That is, the anisotropy in the resistivity between the *a*- and *c*-axes is not known.

Since the thermal reflectance of the  $\kappa$ -(BETS)<sub>2</sub>FeBr<sub>4</sub> samples has been measured in this study, the Hagen-Rubens thermal reflectance (HR(T1)/HR(T2)) was also calculated. In this case, T1 represents different temperatures (T1 = 10 K, 25 K, 30 K, 35 K, 60 K, 80 K) and T2 = 2.8 K is the base temperature. The *ac*- plane dc-resistivity corresponding to the temperatures T1 were  $\rho_{dc} = 0.5, 5.8, 25, 33.3, 75$  and  $58$  m.Ω.cm respectively and that corresponding to T2 = 2.8 K was  $0.2$  m.Ω.cm.

The Hagen-Rubens thermal reflectance plots are shown in Fig. 4.8. These plots correspond to an average over the *ac*-plane and can be compared with the experimental thermal reflectance shown in Figures 4.5 and 4.6 for the *a*- and *c*-axes respectively. Although the trends of the sample thermal reflectance and Hagen-Rubens result look similar, the Hagen-Rubens thermal reflectance at different temperatures is much lower than the experimental thermal reflectance for samples along the *a*- and *c*-axes indicating that the Hagen-Rubens result is not in agreement with thermal reflectance measured on the  $\kappa$ -(BETS)<sub>2</sub>FeBr<sub>4</sub> samples. Thus from equation 1, the conductivity ( $\sigma_{dc}$ ) is higher for the samples. This could be due to wrong resistivity values due to the small size and brittle nature of the samples which introduces cracks, and the fact that the resistivity plot is measured in the *ac*-plane not in a specific direction, or to the fact that the sample reflectance is not obeying Hagen-Rubens equation in the coherent regime (which is the temperature range in which



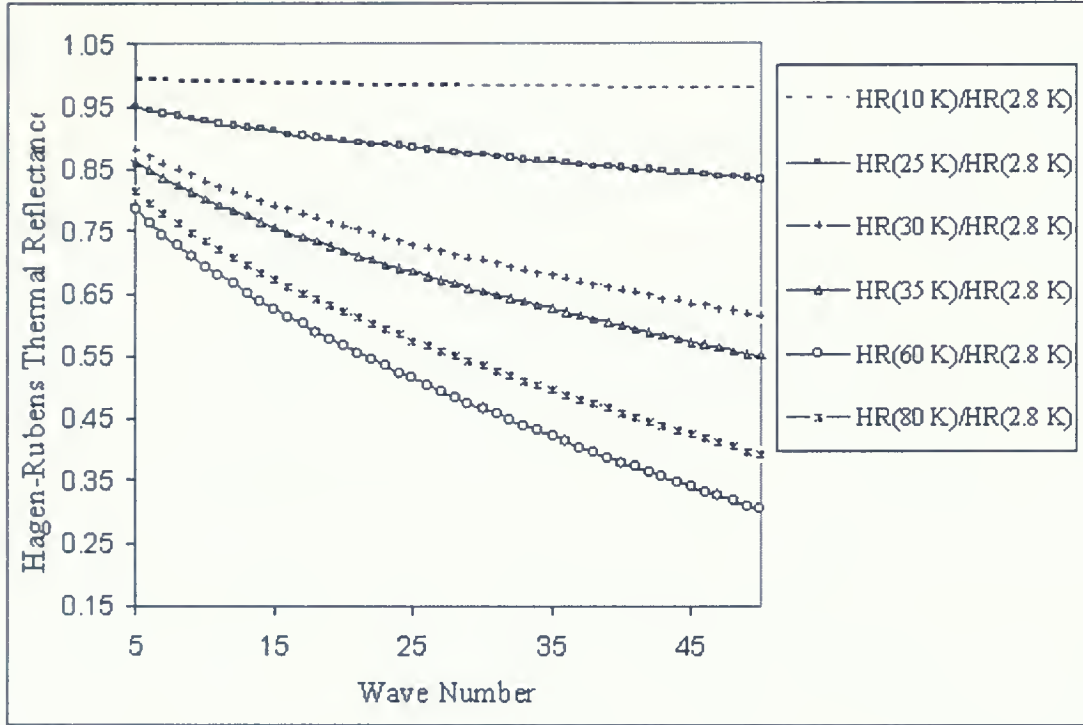


Figure 4.8: Hagen-Rubens thermal reflectance calculation at different temperatures.

the resistivity drops rapidly with decreasing temperature).

As the other members of our group will continue this work, there is a goal to determine the absolute reflectance through measurements over a wide frequency range in order to use Kramer-Kronig analysis to calculate the optical constants  $n$  and  $k$  and therefore  $\epsilon_1$ ,  $\epsilon_2$  (real and imaginary parts of dielectric constant) and  $\sigma_1$  (real part of the conductivity) [22]. Eventually,  $\sigma_1$  could be compared to  $\sigma_{dc}$  which was calculated from the Hagen-Rubens equation to investigate how these two conductivities match at low frequency and how polarization along the easy axis could influence the conductivity.





# Chapter 5

## Conclusions

$\kappa$ -(BETS)<sub>2</sub>FeBr<sub>4</sub> is an interesting compound exhibiting an antiferromagnetic and a superconducting transition at low temperatures.

Optical experiments in the far-infrared frequency range can provide important information on the electronic structure [17]. By using polarized light, one can elucidate the anisotropy in the properties with respect to the orientation of the crystal axes.

Investigation of how the low frequency electromagnetic response is affected by the antiferromagnetic and superconducting states, as well as the onset of strong correlation for  $\kappa$ -(BETS)<sub>2</sub>FeBr<sub>4</sub> samples has been the subject of the present thesis. Polarized thermal reflectance measurements of  $\kappa$ -(BETS)<sub>2</sub>FeBr<sub>4</sub> along the *a*- and *c* axes were carried out using a <sup>3</sup>He refrigerator cryostat and a Martin-Puplett type polarizing interferometer.

Thermal reflectance plots, where the SC state is compared to the normal state, along the *a*- and *c*-axes exhibiting a rise at low frequencies (below 10 cm<sup>-1</sup>) which implies the reflectance in the SC state is higher than that in the normal state. This feature that appears at low frequencies may indicate the energy scale of the superconducting energy gap. The expected zero-temperature BCS energy gap, 2  $\Delta$ , corresponds to 2.5 cm<sup>-1</sup>. The fact that the frequency range of the increased thermal reflectance is higher than that expected from BCS theory suggests that  $\kappa$ -(BETS)<sub>2</sub>FeBr<sub>4</sub> is an unconventional superconductor.

The thermal reflectance plots including the AF state along the *a*- and *c*-axes exhibit a dip-like feature at low frequencies which indicates that the reflectance in the AF state is lower than that in the normal state. The energy scale of the depression at low frequencies (approximately below 15 cm<sup>-1</sup>) may be due to the opening of a gap in the antiferromagnetic state.

Although it has been reported that there is an anisotropy between *a*- and *c*-axes [1], there does not seem to be a significant difference in the low frequency low temperature optical properties along



the easy axis compared to the normal axis.

The thermal reflectance measurements at higher temperatures (10 K-80 K) show that the reflectivity decreases with increasing temperature to 60 K (the coherence temperature) above which it increases again. This trend was expected from the temperature dependence of the electrical resistivity as well. The comparison of the thermal reflectance plots along the  $a$ - and  $c$ -axes at higher temperatures reveals the existence of anisotropy between the two axes.

The Hagen-Rubens thermal reflectance plots (that have been calculated for the  $ac$ -plane using experimental resistivity values [1]) were compared with the experimental thermal reflectance plots obtained along the  $a$ - and  $c$ -axes. While the general trends of the thermal reflectance and Hagen-Rubens results look alike, the Hagen-Rubens thermal reflectance at different temperatures is much lower than the thermal reflectance measured on the  $\kappa$ -(BETS)<sub>2</sub>FeBr<sub>4</sub> samples which implies the  $ac$ -plane dc-conductivity is not consistent with the optical results obtained along particular axes. In future work, the real part of the optical conductivity ( $\sigma_1$ ) could be determined using Kramers-Kronig analysis in order to evaluate the anisotropy in the transport properties.



# Bibliography

- [1] H. Fujiwara, E. Fujiwara, Y. Nakazawa, B. Narymbetov, K. Kato, H. Kobayashi, A. Kobayashi, M. Tokumoto, and P. Cassoux. A Novel Antiferromagnetic Organic Superconductor  $\kappa$ -(BETS)<sub>2</sub>FeBr<sub>4</sub>. *J. Am. Chem. Soc.*, 123:306–314, 2001.
- [2] T. Konoike, S. Uji, T. Terashima, M. Nishimura, S. Yasuzuka, K. Enomoto, , H. Fujiwara, B. Zhang, and H. Kobayashi. Magnetic-Field-Induced Superconductivity in the Antiferromagnetic Organic Superconductor  $\kappa$ -(BETS)<sub>2</sub>FeBr<sub>4</sub>. *Phys. Rev. B*, 70:094514, 2004.
- [3] Ch. Kittel. *Introduction to Solid State Physics*. John Wiley and Sons, 7 edition, 1996.
- [4] T. Ishiguro and K. Yamaji. *Organic Superconductors*. Springer-Verlag, 1989.
- [5] M. Lang and J. Muller. Organic Superconductors. arXiv:cond-mat302157 v1. 2003.
- [6] N. Ashcroft and D. Mermin. *Solid State Physics*. Thomson Learning, 1976.
- [7] H. Kobayashi, H. Tomita, T. Natito, A. Kobayashi, F. Sakai, T. Watanabe, and P. Cassoux. New BETS Conductors with Magnetic Anions (BETS) bis(ethylenedithio)tetraselenafulvalene). *J. Am. Chem. Soc.*, 118:368–377, 1996.
- [8] F. Pratt, S. Lee, S. Blundell, I. Marshall, H. Uozaki, and N. Toyota.  $\mu$ SR Studies of the Interaction between Magnetism and Superconductivity in  $\kappa$ -(BETS)<sub>2</sub>FeCl<sub>4</sub>. *Synthetic Metals*, 133-134:489–492, 2003.
- [9] J. Franklin. *Classical Electromagnetism*. Pearson, 2005.
- [10] E. Fujiwara, V. Gritsenko, H. Fujiwara, I. Tamura, H. Kobayashi, M. Tokumoto, and A. Kobayashi. Magnetic Molecular Conductors Based on BETS Molecules and Divalent Mag-



- netic Anions [BETS = Bis(ethylenedithio)tetraselenafulvalene]. *Inorg.Chem.*, 41:3230–3238, 2002.
- [11] L. Balicas, J. Brooks, K. Storr, D. Graf, S. Uji, H. Shinagawa, E. Ojima, H. Fujiwara, H. Kobayashi, A. Kobayashi, and M. Tokumoto. Shubnikovde Haas Effect and Yamaji Oscillations in the Antiferromagnetically Ordered Organic Superconductor  $\kappa$ -(BETS)<sub>2</sub>FeBr<sub>4</sub>: A Fermiology Study. *Solid State Communications*, 116:557–562, 2000.
- [12] H. Fujiwara, H. Kobayashi, E. Fujiwara, and A. Kobayashi. An Indication of Magnetic-Field-Induced Superconductivity in a Bifunctional Layered Organic Conductor  $\kappa$ -(BETS)<sub>2</sub>FeBr<sub>4</sub>. *J. Am. Chem. Soc.*, 124:6816–6817, 2002.
- [13] M. Tinkham. *Introduction to Superconductivity*. McGraw-Hill, 2nd edition, 1996.
- [14] L. Gupta and M. Multani, editors. *Selected Topics in Superconductivity*. World Scientific, 1993.
- [15] A. Mackenzie. Unconventional Superconductivity. lecture notes, Cambridge Winter School, 2004.
- [16] G. Loudon. *Organic Chemistry*. New York : Oxford University Press, 2002.
- [17] J. Ferraro, J. Thorn, R. Carlson, K. Geiser, U. Wang, H. Kini, and A. Whangbo. *Organic Superconductors*. Springer-Verlag: Berlin, 2nd edition, 1998.
- [18] F. Mena. *Optics and Magnetism: From Itinerant to Localized Electrons*. PhD thesis, University of Groningen, 2004.
- [19] A. Kini, K. Carlson, H. Wang, J. Schlueter, J. Dudek, S. Sirchio, U. Geiser, K. Lykke, and J. Williams. *Physica C*, 264:81, 1996.
- [20] A. Girlando, M. Masino, G. Visentini, A. Brillante, R. Della Valle, and E. Vemuti. *Synth. Met.*, 109:13, 2000.
- [21] *Infrared Laboratories*, 1994. Brock University Instruction Manual.





- 
- [22] M. G. Hildebrand. The Infrared Optical Properties of  $\text{Sr}_2\text{RuO}_4$  and  $\text{SmTiO}_3$  Including an Object-Oriented Resistivity Interface. Master's thesis, Brock University, 1999.
- [23] M. Beat. *Low Temperature Spectroscopy : Optical Properties of Molecules in Matrices ; Mixed Crystals, and Frozen Solutions*. New York : American Elsevier Pub. Co., 1971.
- [24] S. Ocadlik. Far-Infrared Spectroscopy of Heavy Fermion Superconductor  $\text{CeCoIn}_5$ . Master's thesis, Brock University, 2004.
- [25] E. Hecht and A. Zajac. *Optics*. Addison-Wesley Publishing Company, 1979.
- [26] R. Ellison. Far-Infrared Reflectance and Optical Properties of Organic Superconductor  $(\text{TMTSF})_2\text{ClO}_4$ . Master's thesis, Brock University, 2001.
- [27] N. Dennis and T. Heppell. *Vacuum System Design*. London : Chapman Hall, 1968.
- [28] J. Yates. *Experimental Innovations in Surface Science : A Guide to Practical Laboratory Methods and Instruments*. New York : AIP Press : Springer, 1998.
- [29] P. McClintock, D. Meredith, and J. Wigmore. *Low-Temperature Physics*. Blackie Glasgow and London, 1992.
- [30] F. Din and A. Cockett. *Low-Temperature Techniques*. London : G. Newnes, 1960.
- [31] J. Leonard. *Low Temperature Physics*. London : Methuen, 1962.
- [32] D. Bonn, J. Garrett, and T. Timusk. Far-Infrared Properties of  $\text{URu}_2\text{Si}_2$ . *Phys. Rev. Letters*, 61:1305–1308, 1988.
- [33] G. Sudhakar Rao and M. Reedyk. Comparison of the Normal- and Superconducting-State Electromagnetic Absorption in  $\text{Sr}_2\text{RuO}_4$ . *Phys. Rev. B*, 73:052507, 2006.













